

AERODYNAMIC SHAPE OPTIMIZATION OF A BOUNDARY-LAYER INGESTING
S-DUCT INTAKE

by

Christopher Chiang

A thesis submitted in conformity with the requirements
for the degree of Master of Applied Science

Graduate Department of Aerospace Engineering
University of Toronto

Abstract

Aerodynamic Shape Optimization of a Boundary-Layer Ingesting S-Duct Intake

Christopher Chiang

Master of Applied Science

Graduate Department of Aerospace Engineering

University of Toronto

2021

An aerodynamic shape optimization framework based on the Reynolds-averaged Navier-Stokes equations is applied to the optimization of a boundary-layer ingesting S-duct designed for an embedded engine on a high-subsonic, unmanned flight vehicle. Two composite objective functions are considered. The first combines distortion and swirl at the fan interface plane as well as total pressure recovery, with user-defined weights for each objective, while the second involves pressure recovery, fan blade load variation, and fan blade incidence variation. Pareto fronts are generated that demonstrate the trade-offs between objectives. Single-point and multipoint optimizations are conducted at cruise, descent, and climb conditions to evaluate the robustness of the design. Results indicate that compared to the baseline geometry, a simultaneous improvement in all objectives can be obtained, depending on the priorities pre-assigned by the user. Lastly, multipoint optimization results show that a single S-duct geometry can perform well during cruise, climb, and descent conditions.

Acknowledgments

First and foremost, I would like to thank my supervisor, Professor David Zingg, for his support and guidance. I am grateful for the opportunity to work on a unique project that provided many valuable learning experiences. His advice and insight are invaluable contributions to the progression of the research. The passion and drive to progress the knowledge of environmentally-friendly aircraft design and reduce the impact of aviation on climate change are certainly admirable; and serve as an inspiration for myself and others.

I would also like to thank the members of my Research Assessment Committee, Professor Prasanth Nair and Professor Masayuki Yano for their guidance at various stages of this project.

I extend my gratitude to the UTIAS community for welcoming me and for the friendships I have formed with other students. I would like to thank the entire Aerospace Students' Association executive team for their time and effort in organizing enjoyable events for the student body.

To the members of the computational aerodynamics group, I would like to thank you for your camaraderie and for creating a fun, social, and supportive environment to work in. Thanks to Dr. Thomas Reist for his expertise in all things Jetstream or ICEM related. Thank you to several other members of the group, Tim, Gregg, Mike, and Aiden, for sharing your knowledge in insightful conversations and providing mentorship on Jetstream, FFDs, and Diablo.

Lastly, I would like to thank my friends and family. I was fortunate to have been surrounded by friends that made the COVID-19 pandemic all the more bearable. To my sister and most of all, my parents, thank you for all the sacrifices you have made for me and for your unwavering support throughout the years.

Contents

1	Introduction	1
1.1	Motivation	1
1.2	Boundary-Layer Ingestion	2
1.3	S-Duct Intake Design	4
1.3.1	Total Pressure Recovery	5
1.3.2	Intake Flow Distortion	6
1.3.3	Secondary Flow	7
1.4	Pareto Fronts and Trade-Offs	8
1.5	Aerodynamic Shape Optimization	9
1.5.1	Previous Applications to Intakes	10
1.6	Thesis Objectives and Outline	12
2	Methodology	13
2.1	Geometry Parameterization, Control, and Mesh Movement	13
2.1.1	B-Spline Representation	13
2.1.2	Grid Fitting	14
2.1.3	Free-Form Deformation Control	15
2.1.4	Mesh Movement Algorithm	16
2.2	Flow Solver	16
2.3	Optimization Algorithm	17
2.3.1	SNOPT	17
3	Intake Optimization	18
3.1	The Baseline S-Duct	18
3.2	Geometry Parameterization and Control	18
3.3	Flow Solver	20
3.3.1	Boundary-Layer Profile Generation	20
3.3.2	Boundary-Layer Ingestion Implementation	21
3.3.3	Inlet Mach Number Iterative Algorithm	22

3.3.4	Validation for Internal Flows	24
3.4	Intake Optimization Algorithm	24
3.4.1	Optimization Problem Formulation	25
3.4.2	Gradient Evaluation	25
3.5	Multi-Objective Optimization	27
3.5.1	Objective Functions	27
3.5.2	Composite Objective Function Formulation	29
3.5.3	Multipoint Objective Function Formulation	30
3.6	Optimization Parameter Studies	30
3.6.1	Grid Density	30
3.6.2	Investigation of the Impact of the Number of Design Variables	31
3.6.3	Investigation of Geometric Constraints	32
4	Results	36
4.1	Optimization with Pressure Recovery, Distortion, and Swirl	36
4.1.1	Pareto Front Characterization	36
4.1.2	Single-Point Optimization	38
4.1.3	Multipoint Optimization	41
4.2	Optimization with Pressure Recovery and Blade Variation Parameters	46
4.2.1	Pareto Front Characterization	46
4.2.2	Single-Point Optimization	47
4.2.3	Multipoint Optimization	48
4.3	Presence of Multimodality	50
5	Conclusions and Recommendations	54
5.1	Conclusions	54
5.2	Recommendations	55
References		57

List of Tables

3.1	Boundary SATs.	21
3.2	Operating points.	30
3.3	S-duct grid information.	31
3.4	Optimized performance values for pressure recovery, distortion, and swirl with $\alpha = 0.80$ and $\beta = 0.80$ at cruise and different amounts of geometric freedom.	34
4.1	Optimized performance with pressure recovery, distortion, and swirl at cruise and a fan speed of 35,000 RPM.	38
4.2	Performance at multiple operating points optimizing with $\alpha = 1.00$ and $\beta = 0.80$ (PR and D).	42
4.3	Performance at multiple operating points optimizing with $\alpha = 0.95$ and $\beta = 0.90$ (PR , D , and S).	44
4.4	Optimized performance with pressure recovery, blade load variation, and blade incidence variation at cruise and a fan speed of 35,000 RPM.	47
4.5	Performance at multiple operating points optimizing with $\alpha = 0.90$ and $\beta = 1.00$ (PR and ϕ_{var}).	50
4.6	Cruise optimized performance showing multimodality with $\alpha = 0.90$, $\beta = 1.00$ (PR and ϕ_{var}).	52

List of Figures

1.1	M2129 S-duct.	5
1.2	Performance of a typical BLI S-duct at the fan interface plane.	6
1.3	Example of a two-dimensional Pareto front.	9
3.1	Flowchart of Jetstream for intake optimization.	19
3.2	Baseline S-duct performance at cruise.	20
3.3	FFD control volume for the S-duct.	20
3.4	Example of total pressure and turbulent viscosity profiles in the boundary layer.	21
3.5	Example of an inlet Mach number distribution with BLI.	22
3.6	Diablo results for the pressure coefficient compared to numerical and experimental results at an inlet Mach number of 0.8 without BLI. . .	24
3.7	Resultant velocity triangle of a fan blade from radial blade element discretization.	28
3.8	Discretization of the baseline geometry.	31
3.9	Grid convergence for the baseline geometry.	32
3.10	Optimization convergence of FFD with m cross-sections and n -by- n control points denoted as $m \times n \times n$	33
3.11	Optimized geometry and outlet total pressure for pressure recovery, distortion, and swirl with $\alpha = 0.80$ and $\beta = 0.80$ at cruise and different amounts of geometric freedom.	34
4.1	Pareto front for the tri-objective function with pressure recovery, distortion, and swirl at cruise.	37
4.2	Comparison of outlet contours at cruise and a fan speed of 35,000 RPM (PR , D , and S).	39
4.3	Comparison of streamlines at cruise and a fan speed of 35,000 RPM (PR , D , and S).	40
4.4	Comparison of S-duct geometries at cruise and a fan speed of 35,000 RPM (PR , D , and S).	41

4.5	Outlet total pressure contours optimizing with $\alpha = 1.00$, $\beta = 0.80$ (PR and D).	43
4.6	Outlet total pressure contours optimizing with $\alpha = 0.95$, $\beta = 0.90$ (PR , D , and S).	45
4.7	Pareto fronts for the tri-objective function with pressure recovery, blade load variation, and blade incidence variation at cruise and a fan speed of 35,000 RPM.	46
4.8	Comparison of outlet contours at cruise and a fan speed of 35,000 RPM (PR , L_{var} , and ϕ_{var}).	48
4.9	Comparison of streamlines at cruise and a fan speed of 35,000 RPM (PR , L_{var} , and ϕ_{var}).	49
4.10	Comparison of S-duct geometries at cruise and a fan speed of 35,000 RPM (PR , L_{var} , and ϕ_{var}).	49
4.11	Outlet total pressure contours optimizing with $\alpha = 0.90$, $\beta = 1.00$ (PR and ϕ_{var}).	51
4.12	Evidence of multimodality.	52

Chapter 1

Introduction

1.1 Motivation

There is an increasing requirement for the aviation industry to reduce its carbon footprint and its environmental impact on climate change. The emission of carbon dioxide (CO_2) and other constituent greenhouse gases from the combustion of jet fuel contribute to the anthropogenic global warming of the planet, leading to rises in global temperatures, sea level, and more unpredictable and destructive weather disasters. At the altitude at which these emissions are released into the atmosphere, they pose both short term and long term harmful effects to the environment.

Radiative forcing (RF) is one metric that describes the net energy flux in the atmosphere. Positive RF indicates a planet warming effect. Conversely, negative RF cools the planet. From the combustion of jet fuel, aviation emits CO_2 , water vapour, other non- CO_2 gases such as nitrogen oxides (NO_x) and sulfur dioxide, unburnt hydrocarbons and carbon monoxide from incomplete combustion, and soot particulates. In terms of RF, the impact of aviation on climate change is briefly listed below [39]:

- CO_2 emissions result in a positive RF.
- Water vapour emissions result in a positive RF.
- NO_x emissions result in the production of ozone with a positive RF and the destruction of ambient methane with a negative RF. Overall, the result is a net positive RF effect.
- Sulphate particles result in a negative RF.
- Soot particles result in a positive RF.
- Contrail formation, with the right atmospheric conditions, results in a net positive RF.

- Aviation-induced cirrus clouds from diffusing contrails result in a net positive RF.

As of 2018, the global contribution of CO₂ emissions from aviation was approximately 2.4% [38]. But even after the pause from the COVID-19 pandemic, the anthropogenic forcing is expected to rise with the inevitable growth of global aviation. Therefore, it is crucial that continual improvements in fuel efficiency are achieved to ensure that the future of aviation is both environmentally and economically sustainable.

Future aircraft designs demand novel configurations with highly integrated aeropropulsive components to achieve optimal performance in fuel efficiency. The D8 Double Bubble concept was studied by researchers at MIT [26, 62, 63] and features a pair of embedded propulsors in the aft upper fuselage. The NASA STARC-ABL is a conventional tube and wing configuration with an all-electric tail-mounted boundary-layer ingesting (BLI) propulsor. Contributions by Gray *et al.* [24] have advanced the analysis and optimization capabilities for the STARC-ABL using a coupled aeropropulsive approach.

The blended wing body design is one of the configurations that is being researched to evaluate its potential benefit. The NASA N3-X is an example of a blended wing body with distributed BLI propulsion [18, 40]. Compared to a conventional tube and wing configuration with podded engines beneath its wings, this unconventional configuration has the option to embed its engines into the upper surface of the aft fuselage. This allows for BLI and is described in more detail in Section 1.2. However, this coupling introduces complicated aerodynamic interactions and fan-face distortion that decrease engine performance, leading to issues in the reliability of safe operation. Despite the challenges, propulsion airframe integration is an important technology advancement that couples the development of both systems that bring promise to further increase fuel efficiency, reduce emissions, suppress noise, and improve overall aircraft system level performance.

1.2 Boundary-Layer Ingestion

BLI is an aero-propulsive concept in which the propulsor ingests the incoming boundary layer developing over the airframe to improve overall system efficiency, with the intent of improving fuel efficiency. The concept has long been known amongst the research community for its fuel saving potential [7, 36], where applications for marine propulsion in ships and torpedoes have been extensively studied [57]. Its resurgence in recent years is due to renewed interest in applying the concept to highly-integrated aeropropulsive systems for more fuel-efficient aircraft [18, 24, 63], urban air mobility

vehicles [49], and missiles [42].

By ingesting the lower momentum boundary layer, the propulsion system can potentially expend less power than that required by a podded engine. Furthermore, re-energizing the aircraft wake enables less wasted kinetic energy for a given amount of thrust [50]. The complete benefit of BLI can be analyzed through the power balance method developed by Drela [17].

The force analysis of aircraft is traditionally separated into aerodynamic drag and thrust. However, this decomposition can be ambiguous for airframe configurations with tightly integrated propulsion systems. Rather than using a force and momentum analysis, the power balance method focuses on mechanical power and kinetic energy in the flow. The notion of thrust and drag are no longer necessary, as the aerodynamic flow is now quantified into power sources and power sinks.

Applied to airframe configurations, the power balance equation is

$$F_x V_\infty = \Phi_{\text{surf}} + \Phi_{\text{wake}} + \Phi_{\text{vortex}} + \Phi_{\text{jet}} - P_K, \quad (1.1)$$

where the left-hand side is the net propulsive power on the system and the product of the net streamwise force F_x on the body including the propulsors and the freestream velocity V_∞ . At cruise or any other flight condition with a constant speed, the net streamwise force and the net propulsive power is 0. The streamwise force is traditionally accounted for and defined in terms of the surface integral of pressure differences, shear stresses, and momentum fluxes over propulsor inlet and outlet surfaces. The Φ terms quantify various types of power sinks that capture the total viscous dissipation within the system. The Φ_{surf} term is the dissipation due to boundary layers developing on the surface of the body. The Φ_{wake} term involves the trailing wake behind the body. The Φ_{vortex} term is the vortex dissipation and is analogous to the conventional induced drag power. The Φ_{jet} term is the dissipation in propulsor jets. The P_K term is the input mechanical flow power from the engine and is defined only on the propulsor inlet and outlet planes. Therefore, internal losses to the fan performance such as fan efficiency or distortion response are not included in this framework but do not constitute an effect on the external flowfield and net streamwise force [62].

Compared to a conventional podded configuration without BLI within the power balance method, the advantage of an aft-mounted BLI configuration arises from a reduction in the jet and wake dissipation terms, Φ_{jet} and Φ_{wake} respectively. This is due to the propulsors filling in and re-energizing the trailing wake which reduces the wasted kinetic energy left behind the aircraft. As a result, the benefit of BLI propulsion can be quantitatively described as a reduction in the Φ_{jet} and Φ_{wake} terms which translates directly to a reduction in input mechanical flow power P_K required

by the engine to propel the body at the desired freestream velocity V_∞ and net streamwise force F_x .

As an alternative to the force and power balance methods, Arntz *et al.* [3] proposed using an exergy analysis to assess the aero-thermopropulsive performance of future aircraft configurations. The combination of the first and second laws of thermodynamics enables an exergy analysis that splits any form of energy into two parts: the first part that is theoretically fully convertible into mechanical work, adopted as exergy, and the second part that is theoretically impossible to be converted into mechanical work, adopted as anergy. Further details on the theoretical development and application of the exergy analysis can be found in several publications [2, 3, 4].

Lastly, embedding the engine also allows for the inlet to remain flush with the airframe to take advantage of the BLI benefit while also potentially providing some degree of noise suppression. The absence of underwing engine pylons could provide savings in structural weight. There is also a reduction of the wetted surface area of the nacelle compared to that of a podded engine.

1.3 S-Duct Intake Design

The main objective of an air breathing intake is to deliver air at conditions suitable for the engine fan or compressor, supplied at the rate of mass flow required. It accepts the air at an initial freestream Mach number and pressure and diffuses the flow to a lower Mach number and higher pressure. Since the fan face conditions are often at a mismatch from freestream flow conditions, the efficiency of this transformation process drives the design. To avoid any ambiguity, the term “intake” refers to the system that delivers air to the engine while the term “inlet” refers to the entrance of the intake.

Intakes for embedded engines often take the shape of S-ducts. An example of an S-duct is shown in Figure 1.1. The curvature in S-ducts diffuses the air faster than in conventional straight ducts, which leads to more compact designs and potential weight savings. This is also favourable for unmanned aerial and urban air mobility vehicles, as their total size is often determined by the propulsion system [64]. Moreover, the offset lowers the radar and infrared signatures for missiles, which reduces the possibility of detection and increases survivability [32]. With varying S-duct cross-sectional area and shape, the cross-sections can transition from rectangular, oval, semi-elliptical etc. at the entrance to the circular engine face. The centerline curvature of the duct can vary with different offsets and turning angles. S-duct geometries are typically described by the offset and length ratios, based on the engine face diameter, and the

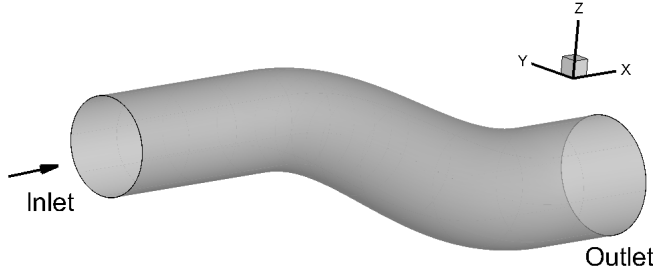


Figure 1.1: M2129 S-duct.

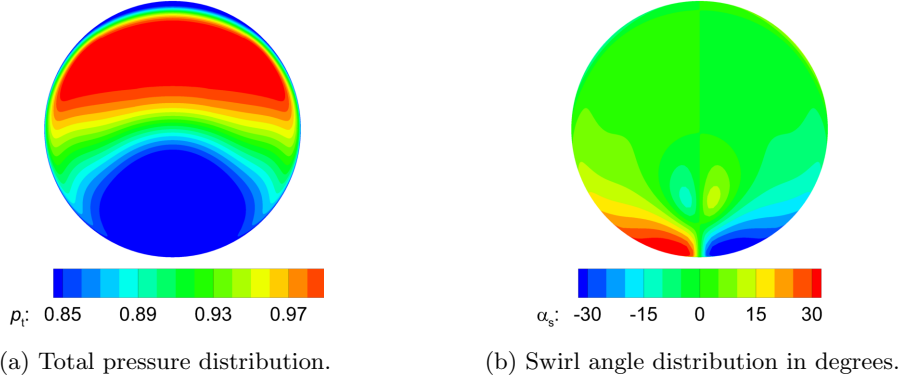
diffusion ratio, which is the ratio of the outlet to inlet areas. An additional aspect ratio is used for rectangular inlets to define their width to height ratio.

1.3.1 Total Pressure Recovery

The total pressure recovery, typically defined as the ratio of the total pressure at the fan interface plane to that at the inlet plane, serves as a measure of efficiency for the intake. Avoiding total pressure losses in the duct is desirable for performance. An efficient intake recovers a large portion of the freestream total pressure at the engine interface by minimizing total pressure losses. Losses can accumulate in three ways. The first is from flow separation, caused by adverse pressure gradients or by aggressive amounts of duct curvature that the flow must follow, leading to turbulent mixing. The second is from friction in the internal duct walls and any external surface that is wetted by the flow going into the duct. The third type of loss occurs from shock waves, which present a considerable challenge in supersonic intakes.

With a podded configuration, intakes are relatively short and the internal flow has a direct route to the engine. Thus, the total pressure recovery is nearly one hundred percent in most cases. However, with an embedded configuration, the intakes are longer with one or more bends and cross-sectional area changes. The total pressure is more susceptible to losses from these geometry changes and friction from the increased wetted surface area.

The pressure recovery has a direct impact on the engine thrust. A general rule of thumb is that in the subsonic region, a 1% decrease in pressure recovery directly translates to a 1% loss in thrust [55, 58]. The proportionality could be greater than unity depending on the engine, and is typically closer to 1.5, especially in supersonic flight [55]. In that regime the relationship becomes increasingly non-linear. For example, at Mach 2.2, a typical engine suffers a 13% reduction in thrust from an 8% loss in pressure recovery [58]. A loss in thrust leads to a reduction in fuel efficiency; hence the importance of pressure recovery in intake design cannot be overstated.



(a) Total pressure distribution. (b) Swirl angle distribution in degrees.

Figure 1.2: Performance of a typical BLI S-duct at the fan interface plane.

1.3.2 Intake Flow Distortion

Maximizing total pressure recovery alone is not typically sufficient for a good design. The total pressure field at the fan face not only needs to be high in an average sense, but it also needs to be uniform. Although a lower average in total pressure recovery can lead to thrust and efficiency penalties, distortions in the total pressure field can reduce fan efficiency, significantly limit engine life due to fan blade fatigue [27], increase noise from fan vibrations, and reduce the surge margin, which compromises engine stability [58]. Since the 1950s, it has been known that intakes with very high average pressure recoveries were not robust. They could be sensitive to off-design conditions that yield higher distortion values over a range of operation than a lower recovery intake [51].

The total pressure at the fan interface plane is shown in Figure 1.2a for a typical BLI S-duct intake. The regions of high total pressure at the top half and low total pressure at the bottom half indicate the extent of distortion in this flow. Total pressure distortion can be described in terms of radial or circumferential distortion. Radial distortion captures the total pressure variation across the blade span from hub to tip. Circumferential distortion is the azimuthal variation in total pressure at a certain span or radius. An experimental study by Reid [53] concluded that radial distortion effects on axial compressors were much less severe than circumferential distortion. It was demonstrated that spoiling a 90° sector of the flow caused a loss in surge pressure ratio that was five times greater than spoiling 25% of the annulus flow. Therefore, circumferential distortion is of primary concern in this thesis, presuming that radial pressure gradients are more easily tolerated by a compressor.

Methods to reduce or control flow distortion in intakes have been the subject of extensive research. Organized into three main categories, the first is by optimization of the geometry, with various types of optimization algorithms being employed.

Geometry optimization attempts to find an optimal shape for the inner walls of the duct. The second is through the use of passive flow control with static devices that delay the onset of boundary-layer separation or prevent it entirely. Fences and vortex generators are mainly used to achieve the desired effect. The devices re-energize the low momentum boundary layer by generating vortical structures that draw higher momentum fluid from the core flow into the boundary layer. This mechanism delays the onset of flow separation and also introduces a secondary flow pattern that ideally counters the formation of the naturally occurring pair of counter rotating vortices [68]. The third category is active flow control that uses boundary-layer suction or blowing. Actuator-controlled jets are typically used to impart additional momentum, requiring approximately 1-2% of the intake mass flow [6, 48]. Wall suction can be achieved with an array of holes upstream of the separation point. A hybrid approach can also be used to leverage the advantages from each category, albeit with additional complexity. Optimization can also be used for the positional placement of passive or active flow control devices.

1.3.3 Secondary Flow

Several documented instances [28, 41, 42, 45] suggest that the two objective design problem of total pressure recovery and distortion may not be adequate in accurately capturing the intake performance over the entire range of operating conditions. Swirl is a secondary flow phenomenon that describes the angularity in the internal flow. Wind tunnel measurements of swirl in an S-duct conducted by Guo and Seddon [25] showed that at high incidence, a large vortex forms around an area of flow separation after the first bend and a pair of counter-rotating vortices in the flow appear after the second bend. This pattern is termed twin or paired swirl. Figure 1.2b demonstrates the swirl angle distribution and the swirl pair at the fan interface plane for a typical BLI S-duct intake.

Frohnnapfel [20] investigated the response of a turbofan engine to simultaneous total pressure and swirl distortion on an experimental test bed. An upstream device simultaneously reproduced combined inlet total pressure and swirl distortion elements in a tailored profile intended to match a defined turbofan engine inlet distortion profile. Under distorted conditions, the specific fuel consumption increased by approximately 5%. An increase in mechanical fan speed was also required, which reduces the stall margin and limits operability. The increase in specific fuel consumption emphasizes the degradation of turbofan system efficiency due to flow distortion and the importance of improving both total pressure and swirl distortion in boundary-layer ingesting intakes.

Historically, the use of inlet guide vanes placed upstream of the fan interface plane avoided many operability problems that did not explicitly account for swirl distortion [1]. Nevertheless, a large amount of swirl can significantly impinge on the incidence angle of inlet guide vanes and induce a cascade effect on the downstream fan and compressors [19]. Depending on the design criteria, these flow control devices are also not always practical due to potential ice accretion modifying the intended performance of the guide vane or foreign object debris being ingested into the engine from a bird strike. In these cases, inlet guide vanes cannot be deployed. Intakes without inlet guide vanes could induce high levels of swirl distortion, leaving the engine vulnerable to compressor stalls and other operability problems [11].

1.4 Pareto Fronts and Trade-Offs

Given the numerous criteria governing intake performance, it becomes increasingly likely that the objectives are competing, meaning that an improvement in one objective requires a sacrifice in another. These trade-offs are highly dependent on the design problem and the complexity increases as the number of objectives increases. To assist in the decision-making process, Pareto fronts are useful in demonstrating quantitative information about the trade-offs amongst competing objectives. Pareto optimality is defined in terms of dominance, meaning that if and only if there does not exist another design that is strictly superior in all objectives, then a design is Pareto optimal [13]. A Pareto optimal design cannot be dominated by other Pareto optimal designs. Therefore, a Pareto front is the locus of Pareto optimal designs. As an example, Figure 1.3 demonstrates two competing objectives J_1 and J_2 that should be both minimized. The curve demonstrates the sacrifice in trading one objective for the other and is discretely represented by five Pareto optimal designs. All designs not on the Pareto front, which is the top right region of the front in the example, are dominated by designs on the front. No designs exist beyond the front, which is the bottom left region of the front in the example.

The designer may have intimate knowledge of their design problem and certain performance objectives to prioritize over others. With a Pareto front, the designer can properly identify the optimal performance that can be achieved based on the weighting placed on each objective. Furthermore, the designer can judge whether the additional price is worth paying in one objective in order to further improve other desired objectives. The designer then has the freedom to adjust their priorities accordingly.

The Pareto front can be generated through a discrete set of optimizations by

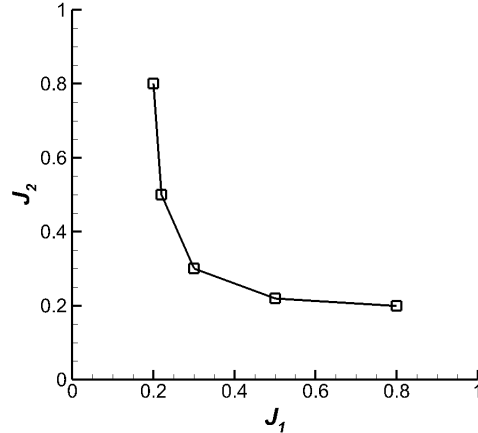


Figure 1.3: Example of a two-dimensional Pareto front.

combining multiple objectives into a single composite objective function, formulated using the weighted sum method. This method introduces parameters that control the weighting of objectives in the objective function. Continuing with the example, the composite objective function is formulated as

$$J = \beta J_1 + (1 - \beta) J_2 . \quad (1.2)$$

Here, the value of β can range from 0 to 1. The composite objective function is then minimized over various values of β . The weighted sum method can be extended to an arbitrary number of objectives, but at most three objectives are simultaneously considered in this thesis.

1.5 Aerodynamic Shape Optimization

This section introduces aerodynamic shape optimization and how it can be leveraged to approach an aerodynamic design problem and utilized to improve performance objectives through numerical methods. The aircraft design process evolved with the advent of powerful numerical analysis tools such as computational fluid dynamics (CFD) and the advancement of efficient and affordable high performance computing. CFD analysis tools, in conjunction with traditional wind tunnel methods, enable an overall increase in the speed and fidelity of aircraft performance predictions. CFD is a well-established field and is capable of modelling many statistically stationary fluid flows around a single design with a relatively high degree of accuracy. Rather than manually analyzing a CFD solution and then iteratively modifying the design, which requires a large amount of effort and expertise from the designer, coupling a CFD solver to a numerical optimization algorithm allows the process to be automated and

iterated until a user-specified performance criterion is obtained or the design cannot be improved any further. The advantage of aerodynamic shape optimization is that its application could reveal novel, unconventional, superior designs that would not have been realized without these numerical algorithms.

Aerodynamic shape optimization algorithms typically comprise a geometry parameterization method, a method to deform the geometry and the mesh, a CFD flow solver, and a numerical optimization algorithm. The user defines the problem by specifying the flow conditions, the objective function that targets a desired aerodynamic performance specification, the geometric freedom given to the optimizer in the form of design variables, and any constraints to be imposed.

In aerodynamic shape optimization, gradient-free and gradient-based optimization algorithms are applicable and widely used. Genetic or evolutionary algorithms [23] are a class of gradient-free methods that can be used to thoroughly search the design space. Analogous to evolution through natural selection, the concept is applied to genetic algorithms that create a new generation that could improve on characteristics from the previous generation through selection, reproduction, and mutation. In the theoretical limit, genetic algorithms are capable of finding the global optimum in a problem where multiple local minima are present.

Although genetic algorithms avoid the calculation of the gradient, they rely heavily on the ability to evaluate the design quickly. However, from a computational standpoint, the evaluation of a flow solution is expensive. Thus, genetic algorithms can be computationally expensive, time-intensive, and impractical for high-fidelity aerodynamic shape optimization.

Gradient-based aerodynamic shape optimization became much more feasible with the introduction of adjoint methods by Jameson *et al.* [33], which allows for the calculation of the sensitivities of aerodynamic functionals with respect to the aerodynamic surface at a computational cost that is independent of the design variables. Gradient-based algorithms make use of the adjoint gradients to search the design space locally. They are efficient and generally require fewer function evaluations compared to genetic algorithms [72]. However, since they descend towards the path defined by the gradient of the objective function, they are susceptible to converge towards a local optimum that is not guaranteed to be globally optimal.

1.5.1 Previous Applications to Intakes

This section briefly describes some previous work in the literature on the aerodynamic shape optimization of intakes. A commonly selected S-duct for optimization is the Royal Aircraft Establishment M2129, introduced by researchers at British Aerospace

Industries in the early 1980s [66, 67] and shown previously in Figure 1.1. It has offset, length, and diffusion ratios of 0.9, 3, and 1.52, respectively. An S-duct optimization studied by Zhang *et al.* [71] featured an irregular bump on the upper wall after the first bend. The intent was to introduce a separated flow region far upstream that helps reduce cross-flow downstream of the duct. The two design parameters were the height and width of the surface perturbation. The objective function was the total pressure distortion at the engine interface. The inflow Mach number was 0.6, the Reynolds number based on the inlet diameter was 2.6 million, and the BLI height was 7.3% of the inlet diameter. Using a gradient-based optimization algorithm, distortion was reduced by 63% compared to the baseline M2129 duct. Pressure recovery remained the same, as the bump behaved like a closed bubble and the separation was confined to that region.

With the same M2129 duct, D'Ambros *et al.* [12] and Chiereghin *et al.* [10] both used the Free Form Deformation (FFD) method [56] to control the S-duct geometry but do not consider BLI. The flow conditions were consistent with those of Zhang *et al.* [71]. Gradient-free genetic algorithms were used to search the design space. Considering pressure recovery and swirl as the two objectives, they were able to achieve considerable improvements over the baseline. Both were able to show parts of a convex Pareto curve that demonstrated the trade-off between pressure recovery and swirl. Lee and Kim [37] used an adjoint method approach to optimize for two separate single objectives at a throat Mach number near 0.85 and a Reynolds number around 7.7 million based on the throat diameter. The first distortion minimization resulted in a 25% reduction from the baseline and the total pressure recovery increased by about 1%. The second optimization was a total pressure recovery maximization, which improved by 1.5% and decreased distortion by 3–7%. They also examined the performance of the design from the second case at several off-design conditions by increasing the Mach number. The optimized duct was able to outperform the baseline in both distortion and pressure recovery at all of the off-design conditions surveyed.

Koo *et al.* [35] developed an aerodynamic shape optimization approach for a fixed rectangular BLI S-duct intake with boundary-layer ingestion, intended for use on a high-subsonic, unmanned flight vehicle. The flight condition was a cruise Mach number of 0.7 and BLI that was 60% of the inlet height. The study was based on steady-state Reynolds-Averaged Navier-Stokes (RANS) simulations, and the geometry was controlled with a free-form deformation volume. The goal of the optimization was to simultaneously maximize total pressure recovery and minimize distortion at the outlet, and they were able to achieve substantial improvements in both objectives. A convex Pareto curve was obtained showing the competing nature between

total pressure recovery and distortion. However, it was observed that the swirl was increased in the optimized ducts compared to the baseline. This suggests that considering total pressure recovery and distortion may not be sufficient, and motivates the addition of swirl into the composite objective function.

1.6 Thesis Objectives and Outline

The objective of this thesis is to build on the work of Koo *et al.* [35] and improve the aerodynamic performance of the S-duct through the application of aerodynamic shape optimization based on the RANS equations. Two different composite objective functions will be investigated. The first is a composite objective function composed of distortion and swirl taken at the fan interface plane and total pressure recovery. The second is a combination of pressure recovery, blade load variation, and blade incidence variation at various fan speeds. With these two composite objective functions, the specific goals are as follows:

1. To generate Pareto fronts to determine the trade-offs between competing objectives.
2. To investigate the robustness of the design and assess the potential performance benefit of S-duct morphing¹ for specific stages of flight against a static multipoint optimized design.

The thesis is organized as follows. Chapter 2 describes the background and methodology of the high-fidelity aerodynamic shape optimization framework called Jetstream. Chapter 3 details the application of Jetstream to internal BLI flows, the formulation of the BLI S-duct intake optimization problem, and the sensitivity of several optimization parameters to the results. Chapter 4 presents the results after applying the aerodynamic shape optimization algorithm to the S-duct design problem. Conclusions and recommendations for future work are detailed in Chapter 5.

¹We do not consider how the morphing is achieved here, only its potential benefits with respect to the considered objectives of the S-duct design.

Chapter 2

Methodology

Jetstream is the optimization software suite that is implemented in this thesis. The methodology for gradient-based aerodynamic shape optimization can be broken down into five main components: geometry parameterization and control, mesh deformation, flow solver, gradient computation, and the optimization algorithm. An overview of the theoretical background for each component is briefly discussed in this chapter.

2.1 Geometry Parameterization, Control, and Mesh Movement

A two-level system of B-splines is used for geometry parameterization and control. The geometry is parameterized by B-spline surfaces defined by B-spline control points. Gagnon and Zingg [21] embedded these B-spline control points within another B-spline volume, called the FFD volume. This second layer provides the distinguishing feature of decoupling parametrization and control with a separate set of design variables, the advantage being that the optimization is able to use fewer design variables. An integrated approach to mesh deformation was developed by Hicken and Zingg [31] using a B-spline volume control mesh for optimization. This section reviews the basic theory behind B-splines, followed by the FFD geometry control system and the details of the mesh movement algorithm.

2.1.1 B-Spline Representation

B-splines can parameterize the geometry in a flexible and efficient manner while preserving an accurate analytical representation of the geometry. A B-spline curve is defined as a piecewise polynomial of degree p or order $p + 1$, expressed as

$$\mathbf{C}(\xi) = \mathcal{N}_i^{(p)}(\xi) \mathbf{B}_i, \quad a \leq \xi \leq b, \quad (2.1)$$

where $\mathcal{N}^{(p)}$ are basis functions weighted by $N + 1$ control points defined as \mathbf{B}_i . The basis functions are defined recursively as

$$\mathcal{N}_i^{(0)}(\xi) = \begin{cases} 1 & \text{if } \xi_i \leq \xi < \xi_{i+1}, \\ 0 & \text{otherwise} \end{cases}, \quad (2.2a)$$

$$\mathcal{N}_i^{(p)}(\xi) = \frac{\xi - \xi_i}{\xi_{i+p} - \xi_i} \mathcal{N}_i^{(p-1)}(\xi) + \frac{\xi_{i+p+1} - \xi}{\xi_{i+p+1} - \xi_{i+1}} \mathcal{N}_i^{(p-1)}(\xi), \quad (2.2b)$$

and are joined at knot locations defined by the knot vector of size $N + p + 1$ written as

$$T = \underbrace{\{0, \dots, 0\}}_{p+1}, \underbrace{\xi_{p+1}, \dots, \xi_N, 1, \dots, 1}_{p+1}. \quad (2.3)$$

The $p + 1$ repeated knots at both ends of the vector ensure that the curve passes exactly through the end control points \mathbf{B}_0 and \mathbf{B}_N . This feature guarantees at least C^0 continuity between distinct B-spline curves and provides a watertight geometry. Extending to multiple dimensions, surfaces and volumes can also be represented with B-splines through tensor products. For example, a B-spline volume is defined as

$$\mathbf{V}(\boldsymbol{\xi}) = \mathcal{N}_i^{(p)}(\xi) \mathcal{N}_j^{(q)}(\eta) \mathcal{N}_k^{(r)}(\zeta) \mathbf{B}_{i,j,k}, \quad (2.4)$$

where $\boldsymbol{\xi} = (\xi, \eta, \zeta)$ are the three-dimensional parametric coordinates.

2.1.2 Grid Fitting

In order to implement the integrated mesh deformation technique, the multi-block structured computational mesh must be fitted with a cubic B-spline volume with a user-specified number of control points. The B-spline parameterization uses spatially varying knot vectors with an equal number of nodes in each knot interval. This yields a B-spline control volume that closely replicates the spatial distribution of the computational mesh. In other words, the control volume is a coarse representation of the computational mesh that is used for the integrated mesh movement scheme which is detailed in Section 2.1.4. The control point coordinates are located using a least squares fit and parameterized first by edges, then surfaces, and lastly volumes. This ordering ensures C^0 continuity between adjacent block interfaces.

Fine off-wall spacings are typically required for an accurate resolution of the boundary layer for the RANS equations. Due to the fine off-wall spacing requirement, there is a tendency during the grid fitting process for the B-spline control points to cluster near the boundary layer. This could result in control point cross-over, leading to cells with negative Jacobians in the control grid and eventually either fitting or

mesh-movement failures. To overcome this problem, the solution is to supply two computational meshes to fit. Both meshes have the same structured blocking topology, number of nodes, and connectivity. The first mesh contains coarsened off-wall spacings with the intention of producing the original B-spline control volume. The second mesh contains refined off-wall spacings suitable for the RANS analysis of turbulent flows. The original B-spline volume control points are frozen while the parameterization along each edge of the second mesh is mapped to the control volume to generate the computational analysis mesh. This approach from Hicken and Zingg [31] avoids control point cross-over arising from fitting excessively fine spacings. Although the generation of two meshes appears to be work-intensive for the user, all that is required is a simple redistribution of nodes in the off-wall direction near the boundary layer on the surface to generate the first coarse mesh.

2.1.3 Free-Form Deformation Control

The FFD concept was pioneered by Sederberg and Parry [56]. Implemented into Jet-stream by Gagnon and Zingg [21], their use of FFD control is advantageous for its ability to provide smooth deformations while maintaining the original analytical definition of the underlying geometry. The generation of FFD volumes is accomplished using a flexible geometry generation tool called GENAIR [21].

In reference to the two-level system, the first level is the FFD volume defined as a lattice of B-spline volume control points. The second level is the B-spline surface control points resulting from the geometry parameterization, which is embedded into the FFD volume of the first level. As the FFD control points deform, the embedded surface control points are deformed along with it. The embedding approach dissociates geometry representation from deformation control, where the FFD volume control points become the geometric design variables. Another important feature is that the mapping is exact, meaning that the sensitivity of the aerodynamic surfaces with respect to the FFD control points does not introduce any error in the gradient for optimization.

Mathematically, the FFD method can be described with two functions. The first function, $F^{-1}(\mathbf{t}) = \boldsymbol{\xi}$, embeds the surface control points \mathbf{t} to parameter space $\boldsymbol{\xi}$ using a Newton search procedure that is only performed once. The second function, $\tilde{F}(\boldsymbol{\xi}) = \tilde{\mathbf{t}}$, handles the deformation of the FFD lattice control points $\mathbf{B}_{i,j,k}$ by algebraically re-evaluating Eq. 2.4 to transform the embedded points in parameter space $\boldsymbol{\xi}$ to the new deformed physical space $\tilde{\mathbf{t}}$. This allows for the geometry to be regenerated quickly once the FFD control system is updated.

2.1.4 Mesh Movement Algorithm

Regenerating the mesh after each design iteration is often computationally expensive or difficult to automate. For these reasons, in Jetstream the preferred method is to use a mesh movement algorithm based on a linear elasticity model developed by Truong *et al.* [61] to deform the existing mesh. To improve robustness and efficiency of the method while maintaining a high mesh quality, Hicken and Zingg [31] applied the algorithm to the coarser, fitted B-spline control mesh rather than directly to the computational mesh. This provides a substantial reduction in computational cost as the number of B-spline volume control points are typically two to three orders of magnitude less than the number of computational mesh nodes.

For this scheme, the mesh movement is typically broken down into a number of linear increments for large shape deformations to improve mesh quality. The control mesh is modelled as a linear elastic solid. The spatially varying Young's modulus is calculated at the beginning of each increment to increase the stiffness in inverse proportion to the volume of each cell as required to preserve mesh quality. For a mesh deformation with m increments, the linear elasticity model produces a system of equations given by

$$\boldsymbol{\mathcal{M}}^{(i)} = \mathbf{K}^{(i)}(\mathbf{b}^{(i)} - \mathbf{b}^{(i-1)}) - \mathbf{f}^{(i)} = 0, \quad i = 1 \dots m, \quad (2.5)$$

where $\boldsymbol{\mathcal{M}}$ are the mesh residuals, \mathbf{K} is the stiffness matrix, \mathbf{b} are the column vectors of volume control points, and \mathbf{f} is the force vector implicitly defined by the displacements of the surface control points. The system is solved using the preconditioned conjugate gradient (PCG) method. The preconditioner is an incomplete lower-upper factorization with a fill level of 1 [44]. Once the design variables have been updated by the optimizer, the embedded B-spline surface control points are deformed accordingly and propagated to the computational mesh through the algebraic relation based on the B-spline mapping.

2.2 Flow Solver

Diablo is a parallel, implicit, multi-block structured finite-difference solver that is used by Jetstream. This Newton-Krylov-Schur flow solver is capable of solving the Euler [29] or the RANS equations [47]. The RANS equations are closed with and fully coupled to the Spalart-Allmaras turbulence model with quadratic constitutive relations [47, 59]. Second-order summation-by-parts operators are used for spatial discretization. Boundary and block interface conditions are enforced weakly through

simultaneous approximation terms [16]. The steady RANS equations are solved in two stages - an approximate-Newton start-up phase for globalization, followed by an inexact-Newton phase for deep convergence. The flexible generalized minimal residual (GMRES) method with an approximate-Schur parallel preconditioner is used to solve the linear system at each Newton iteration. Additional details can be found in Osusky and Zingg [47].

2.3 Optimization Algorithm

A gradient-based formulation is used for the aerodynamic shape optimization algorithm to minimize the objective function, chosen for its computational efficiency and rapid convergence. In this thesis, multiple objectives are considered as defined in Section 3.5.1 and combined to form a composite objective function as described in Section 3.5.2. Although gradient-based methods cannot guarantee convergence to the global optimum, this can be mitigated by applying the gradient-based multi-start method developed by Chernukhin and Zingg [9], which starts the optimization problem from a distinct number of initial conditions that are efficiently sampled using a Sobol sequence [34]. This approach is not considered in this work and only single-start optimization is used. To increase the probability of finding the global optimum, or in most instances a Pareto optimal point, precautions are taken to initialize the optimization problem with a suitable starting geometry to ensure that the best possible optimum is achieved.

Aerodynamic shape optimization problems, especially those in three dimensions, are typically associated with a large number of design variables. For this reason, the discrete adjoint method is employed. The attractive property of the adjoint method is that calculating the gradients comes at a computational cost that is virtually independent of the number of design variables.

2.3.1 SNOPT

The Sparse Nonlinear Optimizer (SNOPT) package is used to solve the optimization problem and provide updated design variables. The mesh is then deformed, followed by the flow, adjoint, and gradient evaluations. To complete the loop, the gradient is fed back in to SNOPT for the next design iteration. SNOPT uses a sequential quadratic programming algorithm and approximates the Hessian using the quasi-Newton Broyden-Fletcher-Goldfarb-Shanno (BFGS) method [46]. The SNOPT algorithm is capable of handling linear and nonlinear constraints, and will satisfy linear constraints exactly. The details of SNOPT are described by Gill *et al.* [22].

Chapter 3

Intake Optimization

A flowchart of Jetstream for intake optimization is shown in Figure 3.1. Several sections in this chapter detail modified processes as they pertain to BLI intakes, followed by optimization parameter studies to investigate their sensitivity to the results.

3.1 The Baseline S-Duct

The geometry denoted herein as the baseline is the S-duct studied by Asghar *et al.* [5] at the Royal Military College of Canada. It features a rectangular inlet with an aspect ratio of 1.5 and an area ratio of 1.57 from the outlet to the inlet. The length-to-diameter ratio is 2.7 with an offset-to-diameter ratio of 1.0.

Figure 3.2 presents the baseline performance at cruise, which demonstrates the non-uniform distribution of high and low total pressure zones at the outlet. The non-uniform circumferential distributions of relative blade loading and relative blade incidence are also shown. As expected, the region of lower relative blade loading and lower relative blade incidence corresponds to the region of low total pressure and the lower axial velocity of the incoming flow. To the right, the streamlines near the boundary layer indicate the presence of secondary flows that generate a pair of counter-rotating vortices downstream of the S-duct at the second bend.

3.2 Geometry Parameterization and Control

The computational domain is parameterized using 4th-order B-spline polynomials and spatially-varying knot vectors [31]. The number of control points is specified by the user in all three directions for each block and is selected to create a suitable fit to the geometry. This B-spline volume forms the control mesh that reduces the number of nodes by approximately two orders of magnitude compared to the computational

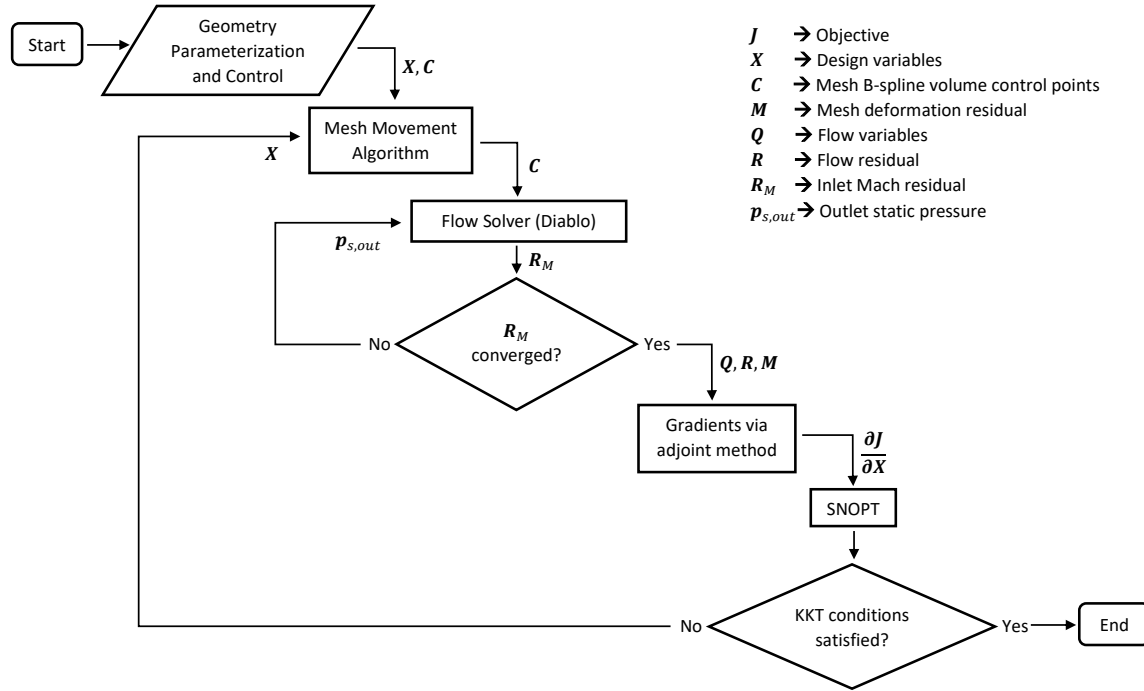


Figure 3.1: Flowchart of Jetstream for intake optimization.

mesh. This allows for more robust and efficient performance for the integrated mesh movement algorithm.

The geometry control scheme for the S-duct is shown in Figure 3.3. The FFD lattice points, shown with 8 cross-sections and 8-by-8 points within each cross-section, are the design variables used for optimization. A study to determine an appropriate number of cross-sections and points to provide adequate geometric flexibility to the optimizer is detailed in Section 3.6.2. Both the inlet and outlet planes, which are clearly not embedded within the FFD volume, are fixed during shape optimization. This also maintains a constant vertical offset between the inlet and outlet faces.

The hydraulic diameter is commonly used as a dimensionless quantity to describe the geometry in non-circular channel and duct flows. It is defined as

$$d_H = \frac{4A_c}{P_w}, \quad (3.1)$$

where A_c is the cross-sectional area of the duct and P_w is the wetted perimeter. Lattice points are restricted to stay within 10% of the hydraulic diameter at their respective cross-section, creating a bounding box for each point. Further exploration of this constraint is discussed in Section 3.6.3. Linear constraints are set to enforce geometric symmetry about the vertical xz -plane, meaning that the movement of a lattice point on the right-half is mirrored on the left-half.

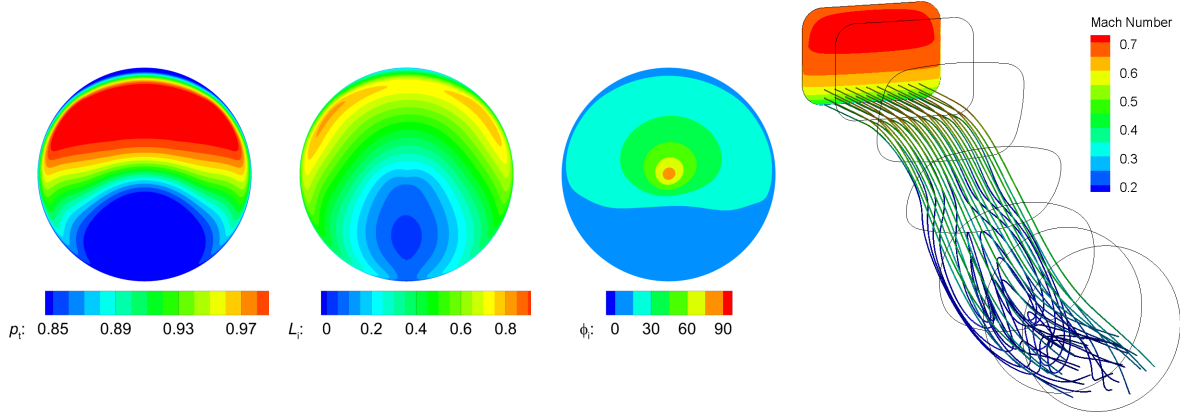


Figure 3.2: Baseline S-duct performance at cruise. Total pressure (left), relative fan blade loading (middle-left), and relative fan blade incidence angle in degrees, (middle-right) at the outlet. Streamlines near the boundary layer (right).

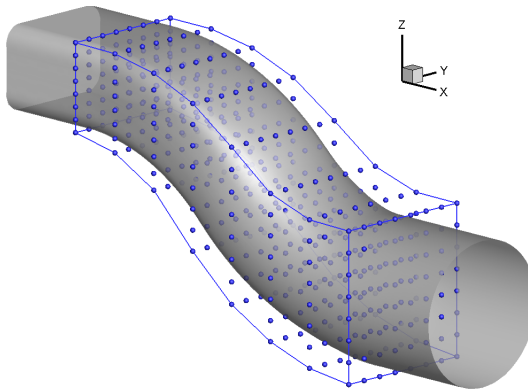


Figure 3.3: FFD control volume for the S-duct.

3.3 Flow Solver

The flow solver Diablo has been used extensively for external flows and validated using the NASA Common Research Model wing-body configuration from the 5th Drag Prediction Workshop [47]. This section describes the modifications that were implemented to adapt the flow solver for internal flows with BLI.

3.3.1 Boundary-Layer Profile Generation

Boundary-layer profiles are generated from a two-dimensional flat-plate flow simulation at the desired Mach number and Reynolds number. The length of the domain is extended until the boundary layer grows to the desired height, defined at the point where the flow velocity reaches 99% of the freestream velocity. The 40-block structured mesh contains approximately 37,000 nodes with a minimum off-wall spacing of 2×10^{-6} of the inlet height.

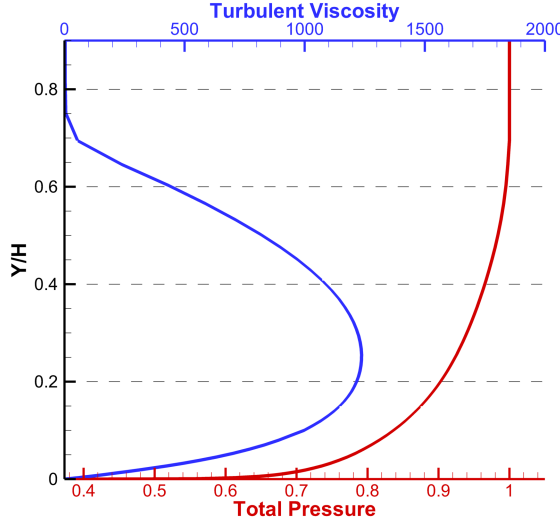


Figure 3.4: Example of total pressure and turbulent viscosity profiles in the boundary layer.

Table 3.1: Boundary SATs.

	Total Pressure Inlet	Static Pressure Outlet
Inviscid SATs	$-H_b^{-1} J^{-1} A_\xi^+ (\mathbf{Q} - \mathbf{Q}_{\text{in}})$	$-H_b^{-1} J^{-1} A_\xi^+ (\mathbf{Q} - \mathbf{Q}_{j+1,k,m})$
Viscous SATs	$\frac{H_b^{-1} \sigma^V}{Re} (\hat{\mathbf{E}}_v)$	$\frac{H_b^{-1} \sigma^V}{Re} (\hat{\mathbf{E}}_v)$
SA Model Advection SATs	$H_b^{-1} \sigma_a (\tilde{\nu} - \tilde{\nu}_{\text{in}})$	$H_b^{-1} \sigma_a (\tilde{\nu} - \tilde{\nu}_{j+1,k,m})$
SA Model Diffusion SATs	$H_b^{-1} \sigma_{df} (g - g_{\text{ff}})$	$H_b^{-1} \sigma_{df} (g - g_{\text{ff}})$

Once the desired boundary-layer height is attained, total pressure and turbulent viscosity profiles are extracted to be applied as boundary conditions described in the following section for the RANS equations and the Spalart-Allmaras turbulence model. An example of the profiles plotted against the normalized inlet height is shown in Figure 3.4.

3.3.2 Boundary-Layer Ingestion Implementation

For internal flows, inlet total pressure and outlet static pressure boundary conditions were implemented through simultaneous approximation terms (SATs) based on the work of Osusky and Zinggg [47]. The boundary SATs are listed in Table 3.1.

From the table, H_b is the boundary node element of the diagonal norm matrix H . J is the metric Jacobian and A_ξ is the flux Jacobian in the ξ direction. The SAT parameter σ_a is to account for the direction of information propagation in the flow.

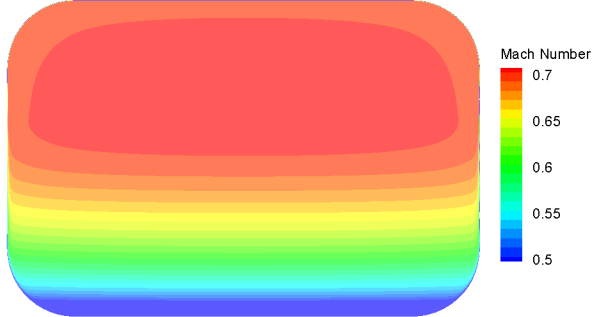


Figure 3.5: Example of an inlet Mach number distribution with BLI.

The SAT parameter σ^V is for viscous fluxes and σ_{df} is for diffusive fluxes. The SA turbulence variable is $\tilde{\nu}$ and g is the gradient of the turbulence variable. \mathbf{Q} is the vector of conservative flow variables and $\hat{\mathbf{E}}_v$ is a viscous flux vector. A more detailed description of the SATs is provided in Osusky and Zingg [47].

Values for the inlet and outlet boundary conditions of the inviscid SATs are calculated based on NASA FUN3D documentation by Carlson [8]. For subsonic inflow, the target flow variables are calculated from isentropic relations using the specified total pressure. Similarly, for the outflow boundary, target flow variables are calculated using the specified outlet static pressure. The spatially varying total pressure and turbulent viscosity profiles are interpolated and applied to the nodes on the inlet face of the S-duct grid. Figure 3.5 shows an example of the Mach number distribution over the inlet plane and the boundary-layer profile with respect to the inlet height after the inlet boundary condition is applied.

3.3.3 Inlet Mach Number Iterative Algorithm

Since the inlet boundary condition enforces total pressure rather than velocity, the outlet static pressure must be adjusted to produce the desired area-averaged inlet Mach number and complete the flow solution. For boundary-layer ingesting flows, only the inlet region above the specified boundary-layer height is considered in the inlet Mach number calculation. Given an initial estimate for the outlet pressure, an algorithm based on the Newton method is used in this work to drive the inlet Mach number towards the desired operating value and converge towards the correct outlet static pressure for a given S-duct geometry. The problem can be formulated as a constrained optimization problem statement with the inlet Mach residual \mathcal{R}_M as the

objective, written as

$$\min \quad \mathcal{R}_M = M_{\text{inlet}}(\mathbf{q}, p_{s,\text{out}}) - M_\infty, \quad (3.2a)$$

$$\text{w.r.t.} \quad p_{s,\text{out}}, \quad (3.2b)$$

$$\text{s.t.} \quad \mathcal{R}(\mathbf{q}, p_{s,\text{out}}) = 0, \quad (3.2c)$$

where $p_{s,\text{out}}$ is the outlet static pressure. The flow residual \mathcal{R} represents the discretized steady RANS equations that must be solved in order to obtain a converged solution for the non-dimensional flow variables \mathbf{q} .

The Lagrangian function is introduced as

$$\mathcal{L} = \mathcal{R}_M + \boldsymbol{\Omega}^T \mathcal{R}(\mathbf{q}, p_{s,\text{out}}), \quad (3.3)$$

where $\boldsymbol{\Omega}^T$ is a Lagrange multiplier. The Karush-Kuhn-Tucker (KKT) conditions must be satisfied for optimality [46], obtained by setting the partial derivatives of \mathcal{L} equal to zero. Setting the partial derivatives of \mathcal{L} with respect to \mathbf{q} and $p_{s,\text{out}}$ to zero yields

$$\left(\frac{\partial \mathcal{R}}{\partial \mathbf{q}} \right)^T \boldsymbol{\Omega} = - \left(\frac{\partial \mathcal{R}_M}{\partial \mathbf{q}} \right)^T, \quad (3.4)$$

$$\frac{d\mathcal{R}_M}{dp_{s,\text{out}}} = \boldsymbol{\Omega}^T \frac{\partial \mathcal{R}}{\partial p_{s,\text{out}}}. \quad (3.5)$$

Eq. 3.4 is a flow adjoint equation, where the first term on the left-hand side is the flow Jacobian matrix. The flow adjoint system is solved using a flexible variant of GCROT [14, 15, 30]. Following the solution for $\boldsymbol{\Omega}$, its dot product with the scalar derivative in Eq. 3.5 produces the total derivative that is used in the formulation for the Newton method to find the correct static pressure, written as

$$p_{s,\text{out},i+1} = p_{s,\text{out},i} + \mathcal{R}_M \left(\frac{\partial \mathcal{R}_M}{\partial p_{s,\text{out}}} \right)^{-1}. \quad (3.6)$$

In practice, provided with a good initial guess, only one to two Newton iterations are typically required to converge the inlet Mach residual to a user-set tolerance of 10^{-5} and complete the flow solution. For an optimization, this algorithm is called upon at each design iteration when a flow solve is required. Since the optimizer gradually adjusts the S-duct geometry, the previous outlet static pressure is typically a strong initial guess for the next design iteration.

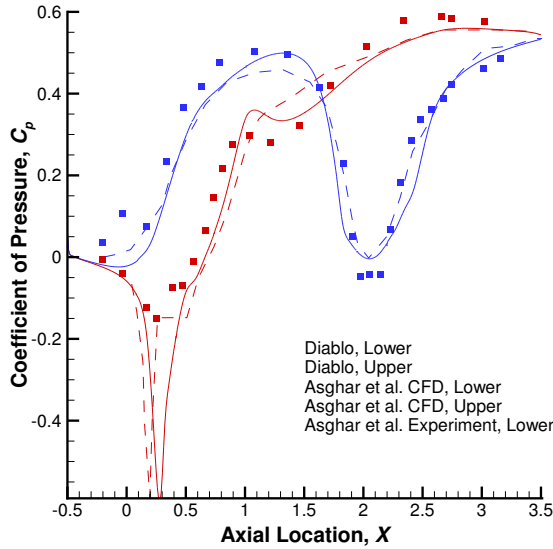


Figure 3.6: Diablo results for the pressure coefficient [35] compared to numerical and experimental results from Asghar *et al.* [5] at an inlet Mach number of 0.8 without BLI. Reproduced with permission.

3.3.4 Validation for Internal Flows

Figure 3.6 displays a plot of the pressure coefficient on the upper and lower surfaces of the S-duct, compared to both CFD and experimental results. The experimental and CFD results for the baseline geometry from Asghar *et al.* [5] were used to validate the flow solver for this class of problem. Note that this validation does not consider BLI and is at an inlet Mach number of 0.8 and a Reynolds number of 1 million. For the purpose of optimization, the level of improvement achieved is several times larger than the error in accuracy. Hence, there is sufficient agreement, indicating that the Spalart-Allmaras turbulence model is adequate for this class of flows, consistent with the conclusions of Yaras and Grosvenor [70].

3.4 Intake Optimization Algorithm

This section details the optimization problem at hand and the gradient calculation with respect to the design variables, subject to a number of constraints.

3.4.1 Optimization Problem Formulation

The optimization problem is formulated as

$$\min \quad \mathcal{J} = (\mathbf{v}, \mathbf{b}^{(m)}, \mathbf{q}, p_{s,out}), \quad (3.7a)$$

$$\text{w.r.t.} \quad \mathbf{v}, \quad (3.7b)$$

$$\text{s.t.} \quad \mathbf{\mathcal{M}}^{(i)}(\mathbf{v}, \mathbf{b}^{(i)}) = 0, \quad i = 1, 2, \dots, m, \quad (3.7c)$$

$$\mathbf{\mathcal{R}}(\mathbf{v}, \mathbf{b}^{(m)}, \mathbf{q}, p_{s,out}) = 0, \quad (3.7d)$$

$$\text{and} \quad M_{\text{inlet}}(\mathbf{v}, \mathbf{b}^{(m)}, \mathbf{q}, p_{s,out}) = M_{\infty}, \quad (3.7e)$$

where \mathcal{J} is the objective function, \mathbf{v} is the vector of design variables, $\mathbf{b}^{(m)}$ are the deformed B-spline control points, \mathbf{q} are the flow variables, and $p_{s,out}$ is the outlet static pressure. The first constraint is the mesh deformation residual $\mathbf{\mathcal{M}}$ at increment i , which is a set of m linear equations that are solved to obtain the B-spline volume control points that control the mesh at the i th increment. The second is the flow residual $\mathbf{\mathcal{R}}$. The last constraint gives the inlet Mach residual $\mathbf{\mathcal{R}}_M$ and ensures the area-averaged inlet Mach number satisfies the specified operating condition. This is done iteratively using the algorithm described in Section 3.3.3. All residuals are theoretically driven to zero, meaning that they converge to machine zero or to a user-defined tolerance for the inlet Mach residual. Additional linear and nonlinear equality and inequality constraints can be included, if required.

3.4.2 Gradient Evaluation

The Lagrangian of the objective function \mathcal{J} is introduced as

$$\begin{aligned} \mathcal{L} = & \mathcal{J}(\mathbf{v}, \mathbf{b}^{(m)}, \mathbf{q}, p_{s,out}) + \sum_{i=1}^m \boldsymbol{\lambda}^{(i)T} \mathbf{\mathcal{M}}^{(i)}(\mathbf{v}, \mathbf{b}^{(i)}) + \\ & \boldsymbol{\psi}^T \mathbf{\mathcal{R}}(\mathbf{v}, \mathbf{b}^{(m)}, \mathbf{q}, p_{s,out}) + \phi^T \mathbf{\mathcal{R}}_M(\mathbf{v}, \mathbf{b}^{(m)}, \mathbf{q}, p_{s,out}), \end{aligned} \quad (3.8)$$

where $\{\boldsymbol{\lambda}^{(i)}\}_{i=1}^m$, $\boldsymbol{\psi}$, and ϕ are the Lagrange multipliers or adjoint variables. The mesh deformation, flow, and inlet Mach residuals are imposed as constraints. The KKT conditions for this problem are slightly more involved with the presence of the inlet Mach residual and the dependence on $p_{s,out}$. For this reason, the augmented adjoint formulation presented by Rashad and Zingg [52] is used here in a similar manner. Setting the partial derivatives of \mathcal{L} with respect to \mathbf{q} and $p_{s,out}$ to zero yields two flow

adjoint equations, formulated as

$$\left(\frac{\partial \mathcal{R}}{\partial \mathbf{q}} \right)^T \boldsymbol{\psi} + \left(\frac{\partial \mathcal{R}_M}{\partial \mathbf{q}} \right)^T \phi = - \left(\frac{\partial \mathcal{J}}{\partial \mathbf{q}} \right)^T, \quad (3.9)$$

$$\left(\frac{\partial \mathcal{R}}{\partial p_{s,out}} \right)^T \boldsymbol{\psi} + \left(\frac{\partial \mathcal{R}_M}{\partial p_{s,out}} \right)^T \phi = - \left(\frac{\partial \mathcal{J}}{\partial p_{s,out}} \right)^T. \quad (3.10)$$

A direct substitution of Eq. 3.4 into Eq. 3.9 produces

$$\left(\frac{\partial \mathcal{R}}{\partial \mathbf{q}} \right)^T \tilde{\boldsymbol{\psi}} = - \left(\frac{\partial \mathcal{J}}{\partial \mathbf{q}} \right)^T, \quad (3.11a)$$

$$\tilde{\boldsymbol{\psi}} = \boldsymbol{\psi} - \boldsymbol{\Omega} \phi. \quad (3.11b)$$

The solution for $\tilde{\boldsymbol{\psi}}$ in 3.11a can be evaluated using the same method as Eq. 3.4. Introducing $\tilde{\boldsymbol{\psi}}$ as a Lagrange multiplier gives

$$\frac{d\mathcal{J}}{dp_{s,out}} = -\tilde{\boldsymbol{\psi}}^T \frac{\partial \mathcal{R}}{\partial p_{s,out}}, \quad (3.12)$$

where the left-hand term can be readily evaluated. Eq. 3.10 can be reduced to the scalar equation written as

$$\frac{d\mathcal{R}_M}{dp_{s,out}} \phi = \frac{d\mathcal{J}}{dp_{s,out}}, \quad (3.13)$$

which provides the value for ϕ . Lastly, the flow adjoint variable $\boldsymbol{\psi}$ is evaluated from Eq. 3.11b.

Setting the partial derivative $\partial \mathcal{L}/\partial \mathbf{b}^{(i)} = 0$ yields the mesh adjoint system, written as

$$\left(\frac{\partial \mathcal{M}^{(m)}}{\partial \mathbf{b}^{(m)}} \right)^T \boldsymbol{\lambda}^{(m)} = - \left(\frac{\partial \mathcal{J}}{\partial \mathbf{b}^{(m)}} \right)^T - \left(\frac{\partial \mathcal{R}}{\partial \mathbf{b}^{(m)}} \right)^T \boldsymbol{\psi} - \left(\frac{\partial \mathcal{R}_M}{\partial \mathbf{b}^{(m)}} \right)^T \phi \quad (3.14)$$

for the final mesh movement increment, and for the preceding increments,

$$\left(\frac{\partial \mathcal{M}^{(i)}}{\partial \mathbf{b}^{(i)}} \right)^T \boldsymbol{\lambda}^{(i)} = - \left(\frac{\partial \mathcal{M}^{(i+1)}}{\partial \mathbf{b}^{(i)}} \right)^T \boldsymbol{\lambda}^{(i+1)}, \quad i = m-1, \dots, 1. \quad (3.15)$$

The solution of the mesh adjoint system is computationally inexpensive, since the size of the system is related to the control mesh and not the computational mesh. Similar to the linear system resulting from mesh movement, the mesh adjoint system is solved using the PCG method described in Section 2.1.4.

To compute the gradient, the adjoint equations are solved sequentially in the order presented. As the constraints are satisfied at optimality, the final KKT condition

$\partial\mathcal{L}/\partial\mathbf{v} = 0$ yields the gradient of the objective function:

$$\mathcal{G} = \frac{\partial\mathcal{L}}{\partial\mathbf{v}} = \frac{\partial\mathcal{J}}{\partial\mathbf{v}} + \sum_{i=1}^m \boldsymbol{\lambda}^{(i)\text{T}} \frac{\partial\mathcal{M}^{(i)}}{\partial\mathbf{v}} + \boldsymbol{\psi}^{\text{T}} \frac{\partial\mathcal{R}}{\partial\mathbf{v}} + \boldsymbol{\phi}^{\text{T}} \frac{\partial\mathcal{R}_M}{\partial\mathbf{v}}. \quad (3.16)$$

3.5 Multi-Objective Optimization

3.5.1 Objective Functions

Intake performance is typically evaluated based on the total pressure recovery ratio that describes the total pressure loss in the duct. Total pressure recovery is defined as

$$PR = \frac{p_{t,\text{out}}}{p_{t,\text{in}}}, \quad (3.17)$$

which is an efficiency metric that should be maximized. Circumferential flow distortion is also significant since it can negatively impact engine performance. Circumferential flow distortion at the outlet is calculated as

$$D = \sum_j^m \sum_i^{n_j} \frac{(p_{t,i} - p_{t,\text{avg},j})^2 dA_i}{A_j}. \quad (3.18)$$

The outlet plane is partitioned into $j = 1, \dots, m$ rings, each with n_j discrete elements. Within each ring, the area-weighted sum of squared error of total pressure is calculated. The total pressure is non-dimensionalized by a free stream normalizing pressure, $\rho_\infty(a_\infty)^2$. The reference velocity u_∞ is replaced by the reference speed of sound, since u_∞ could be zero for some flow problems.

Intakes can also generate significant flow angularity in secondary flows, otherwise known as swirl distortion. In this thesis, the swirl is defined as the angle (in radians) between the circumferential component of the local velocity vector and the axial vector normal to the outlet. The swirl angle is calculated as

$$\alpha_s = \arctan \left(\frac{U_\theta}{U_x} \right). \quad (3.19)$$

The swirl is integrated over the outlet plane, calculated as

$$S = \frac{1}{A_{\text{rings}}} \sum_j^m \sum_i^{n_j} |\alpha_{s,i}| dA_i, \quad (3.20)$$

with the same partitioning of rings and discrete elements that is used in Eq. 3.18. The magnitude of the swirl angle is used as opposed to the directionality since it is a value more suitable for optimization.

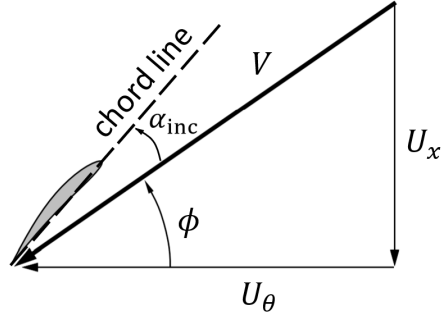


Figure 3.7: Resultant velocity triangle of a fan blade from radial blade element discretization.

Alternative performance metrics are derived to describe the circumferential variation of fan blade loading (i.e. lift) and angle of incidence that a single fan blade would experience through one rotation. Minimizing blade load variation is intended to ease the circumferential loading of the fan blade in light of aerostructural concerns. Minimizing blade incidence variation enables the design of more optimal blade airfoil sections. From blade element theory, the fan blade is radially discretized into independent 2D sections. The resultant velocity triangle in Figure 3.7 shows the axial, tangential, and relative induced velocity components. For this objective function the fan speed must be specified. If the fan speed is variable, multi-point optimization can be applied. Representative fan speeds for this application are modeled after the Williams F107 small turbofan engine, with an upper limit of approximately 35,000 RPM [65]. Moreover, the effect of the fan on the flow in the duct is ignored in this study. No fan blades are modeled and no source terms are used in the simulation; only the tangential velocity contribution of the blade is captured in the calculations of relative angle ϕ and relative velocity V .

The local blade load variation at each radial point includes only the portion of the lift per unit area that varies circumferentially and excludes the contribution from constants. Similarly, the local blade incidence variation considers the variation in the relative angle of attack since the blade metal angle is constant. The relative angle ϕ (in radians) is used to describe the variation in blade incidence instead of α_{inc} as the variation of both angles is the same. These variations are formally defined at each element i as

$$L_i = \rho_i V_i^2 \phi_i \quad (3.21)$$

and

$$\phi_i = \arctan \left(\frac{U_x}{U_\theta} \right), \quad (3.22)$$

respectively. Similar to total pressure distortion, to form a scalar objective, the

circumferential variation in blade loading is written as

$$L_{\text{var}} = \sum_j^m \sum_i^{n_j} \frac{(L_i - L_{\text{avg},j})^2 dA_i}{A_j}. \quad (3.23)$$

The circumferential variation in blade incidence is written as

$$\phi_{\text{var}} = \sum_j^m \sum_i^{n_j} \frac{(\phi_i - \phi_{\text{avg},j})^2 dA_i}{A_j}. \quad (3.24)$$

3.5.2 Composite Objective Function Formulation

For multi-objective optimization, the weighted-sum method is used due to its simplicity and ease of implementation. Two separate composite objective functions are considered in this thesis. A tri-objective function with total pressure recovery, distortion, and swirl is formed such that

$$\mathcal{J}_1 = \alpha\beta \frac{P_{t,\text{out},0}}{P_{t,\text{out}}} + (1 - \beta) \frac{D}{D_0} + \beta(1 - \alpha) \frac{S}{S_0}, \quad (3.25)$$

where the relative weights between all three objectives are determined by α and β . The subscript 0 is the initial value used to normalize each objective, which is typically the baseline value. Since the inlet shape and total pressure are fixed, minimizing the first term is equivalent to minimizing the total pressure losses at the outlet. Note that with special values of α and β , several single- and bi-objective functions can be obtained. With $\alpha = 0$, pressure recovery does not factor into the objective and the relative weighting between distortion and swirl is determined entirely by β . Similarly, an α value of 1 yields a bi-objective function with pressure recovery and distortion. Setting β equal to 1 gives a bi-objective function with pressure recovery and swirl, while a β value of 0 provides a single-objective function to minimize distortion. Setting α and β to 1 solely maximizes pressure recovery, while the combination of $\alpha = 0$ and $\beta = 1$ gives a single-objective minimization of swirl.

The second composite objective function seeks to maximize pressure recovery while simultaneously minimizing the circumferential variation of blade loading and blade incidence, written as

$$\mathcal{J}_2 = \alpha\beta \frac{P_{t,\text{out},0}}{P_{t,\text{out}}} + (1 - \beta) \frac{L_{\text{var}}}{L_{\text{var},0}} + \beta(1 - \alpha) \frac{\phi_{\text{var}}}{\phi_{\text{var},0}}. \quad (3.26)$$

A set of points on a Pareto front can be generated by varying the relative weights between 0 and 1. Although this approach can have difficulty with concave fronts, for

Table 3.2: Operating points.

	Reynolds No.	Mach No.	Boundary-Layer Height	Fan RPM
Cruise	1×10^6	0.7	60% inlet height	35.0×10^3
Descent	1×10^6	0.6	60% inlet height	31.5×10^3
Climb	5×10^5	0.3	80% inlet height	38.5×10^3

example, this was not an issue in this thesis.

3.5.3 Multipoint Objective Function Formulation

Objective functions for multipoint optimizations are discussed in this section. Table 3.2 summarizes the three operating points considered. Note that the rightmost column containing fan RPM values is used exclusively for objective functions containing blade load or blade incidence variation. Two objective functions are formulated for multipoint optimization. The first is written as

$$\mathcal{J}_{\text{mp1}} = 0.5\mathcal{J}_{\text{cruise}} + 0.25\mathcal{J}_{\text{descent}} + 0.25\mathcal{J}_{\text{climb}}, \quad (3.27)$$

where cruise is prioritized twice as much as descent and climb. This will be referred to as multipoint 1 with a 2:1:1 ratio in the results in Chapter 4. The second is written as

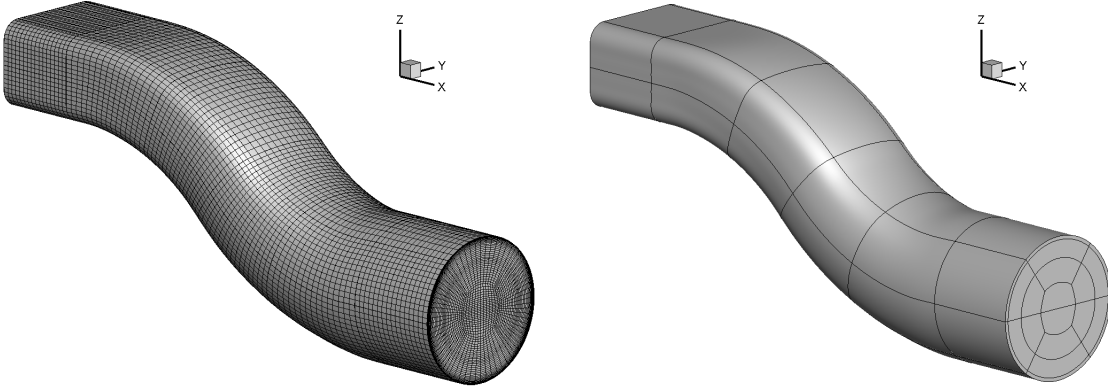
$$\mathcal{J}_{\text{mp2}} = 0.75\mathcal{J}_{\text{cruise}} + 0.125\mathcal{J}_{\text{descent}} + 0.125\mathcal{J}_{\text{climb}}, \quad (3.28)$$

where cruise is weighted six times as much as descent and climb. Similarly, this formulation will be referred to as multipoint 2 with a 6:1:1 ratio in the results. These weights were chosen under the assumption that, in most BLI applications, cruise is the dominant design condition. Two objective functions are chosen in order to assess the sensitivity of the performance to the weighting. Each composite function with operating conditions at cruise, descent, and climb on the right-hand side of Eq. 3.27 and Eq. 3.28 has its own initial values for normalizing the objectives.

3.6 Optimization Parameter Studies

3.6.1 Grid Density

To evaluate the sensitivity of the S-duct performance metrics to grid refinement, a grid density study is completed for the baseline geometry using four grids that range in size from 377,000 to 21 million nodes, labelled from L0 to L3 accordingly. The structured multi-block grid, L1, is shown in Figure 3.8a, with the O-topology



(a) Computational grid used for optimization.

(b) O-grid blocking topology.

Figure 3.8: Discretization of the baseline geometry.

Table 3.3: S-duct grid information.

Grid	Nodes	Average Off-Wall Spacing	Average y^+
L0	3.77×10^5	2.60×10^{-5}	0.68
L1	2.71×10^6	1.16×10^{-5}	0.26
L2	5.19×10^6	1.01×10^{-5}	0.22
L3	21.70×10^6	6.12×10^{-6}	0.13

Average off-wall spacings in units of diameter.

partitioned into 120 blocks as shown in Figure 3.8b. Mesh statistics are detailed in Table 3.3.

The results of each objective are plotted in Figure 3.9, along with values obtained using Richardson extrapolation [54]. The blade incidence variation objective does not show monotonic convergence. This may be due to the inability of the coarsest grid to capture the blade incidence variation accurately due to insufficient discrete elements within a ring that could produce error cancellation from poorly resolved values.

The error for pressure recovery is less than one percent on all grids, while the error for blade incidence variation is less than five percent on all grids. The errors are much larger for distortion, swirl, and blade load variation, as much as 18% using the coarsest grid. Thus, for optimizations it was found that a reasonable balance between accuracy and computational cost is to use the L1 grid, which is the second point from the right in Figure 3.9.

3.6.2 Investigation of the Impact of the Number of Design Variables

The number of cross-sections and the number of control points within each cross-section of the FFD volume are investigated to determine a set that yields an adequate amount of geometric freedom to the optimizer. This study aims to provide additional

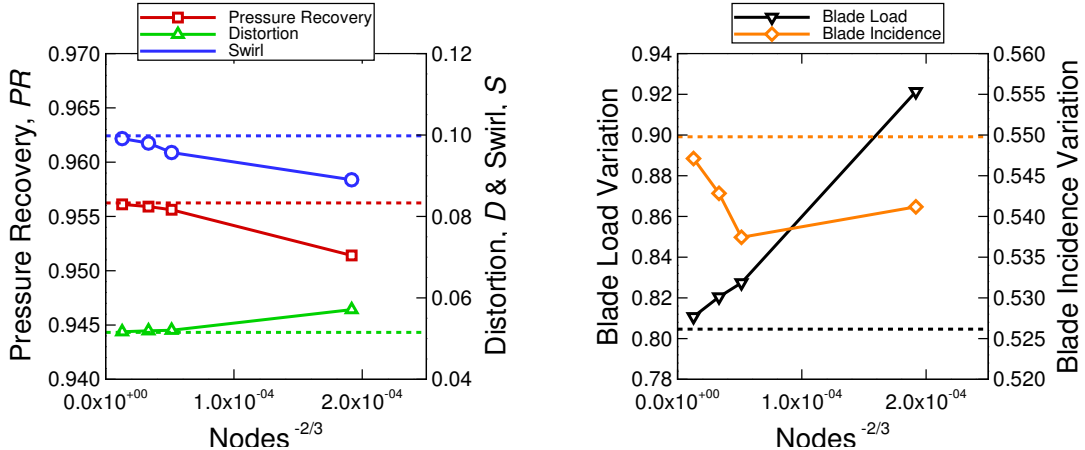


Figure 3.9: Grid convergence for the baseline geometry. Dashed lines indicate the Richardson extrapolated values.

information about the sensitivity of the optimization to the FFD control system and its response to input changes to the FFD volume definition. Three cases are considered, with the first using the composite objective function with pressure recovery, distortion, and swirl with $\alpha = 0.95$ and $\beta = 0.90$. The next case uses the composite objective function with pressure recovery and blade load variation with $\alpha = 1.00$ and $\beta = 0.90$. The final case considers pressure recovery and blade incidence variation with $\alpha = 0.95$ and $\beta = 1.00$. For each case, the number of cross-sections varies from 6 to 12, while the number of control points at each cross-section is varied from 4-by-4 up to 10-by-10.

Figure 3.10 shows the results of the optimization runs for each case. Based on the three plots, there is no significant improvement gained by adding either more axial control sections or more cross-sectional control points past the $8 \times 8 \times 8$ case. Hence, an FFD volume with 8 cross-sections and 8-by-8 control points in each cross-section was selected for all subsequent studies described in this thesis.

3.6.3 Investigation of Geometric Constraints

This section investigates the geometric freedom at each control point of the FFD, which are the design variables of the optimization. The design variables are bounded by a box within their respective cross-section. The extents of the bounding boxes are expressed as a percentage of the hydraulic diameter at each cross-section and constrained such that axial, out-of-plane movements are not permitted. Following the results of the previous FFD volume definition study in Section 3.6.2, an FFD consisting of 8 cross-sections with 8-by-8 control points is used here. For this study, we consider only the composite objective function with pressure recovery, distortion,

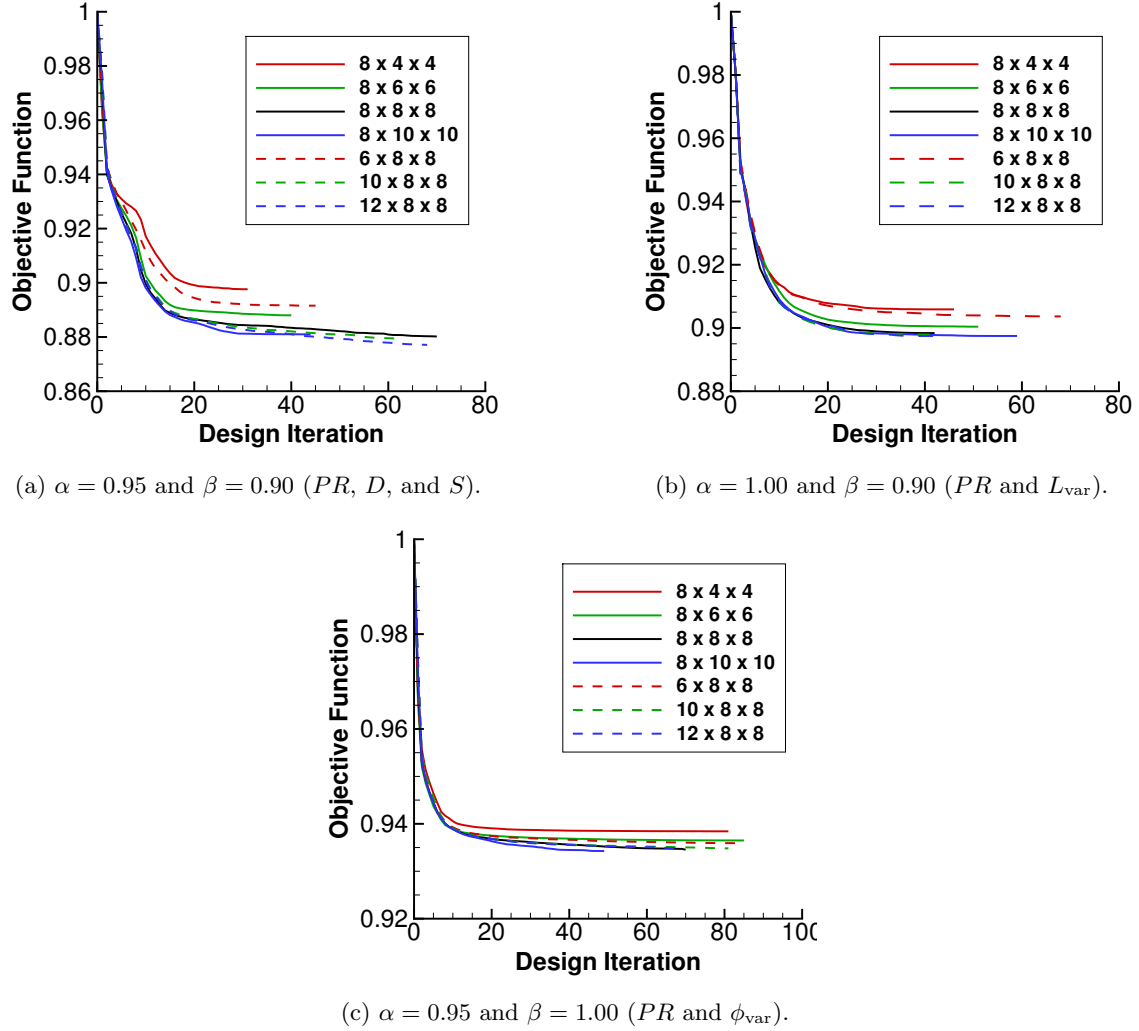


Figure 3.10: Optimization convergence of FFD with m cross-sections and n -by- n control points denoted as $m \times n \times n$.

and swirl with α and β values of 0.80.

The objective function value and the optimized performance values are shown in Table 3.4 for the set of three design variable bounds investigated. There is further improvement in the objective function as the bounds are increased. Given this pair of α and β weights, the optimizer trades pressure recovery for lower amounts of distortion and swirl with the increased geometric freedom.

Figure 3.11 presents the three examples of the optimized geometries with various box constraint values. In Figure 3.11a, the optimizer was evidently not given sufficient design variable freedom. Given the limited design space, it produced a geometry that still displayed pre-existing flow features from the baseline, namely the regions of high total pressure in the top half of the outlet and the low total pressure region in the

Table 3.4: Optimized performance values for pressure recovery, distortion, and swirl with $\alpha = 0.80$ and $\beta = 0.80$ at cruise and different amounts of geometric freedom.

Bounds	J	PR	$D \times 10^2$	$S \times 10^2$
$0.05d_H$	0.7528	0.9635	3.028	0.297
$0.1d_H$	0.6725	0.9536	0.503	0.329
$0.2d_H$	0.6589	0.9426	0.260	0.095

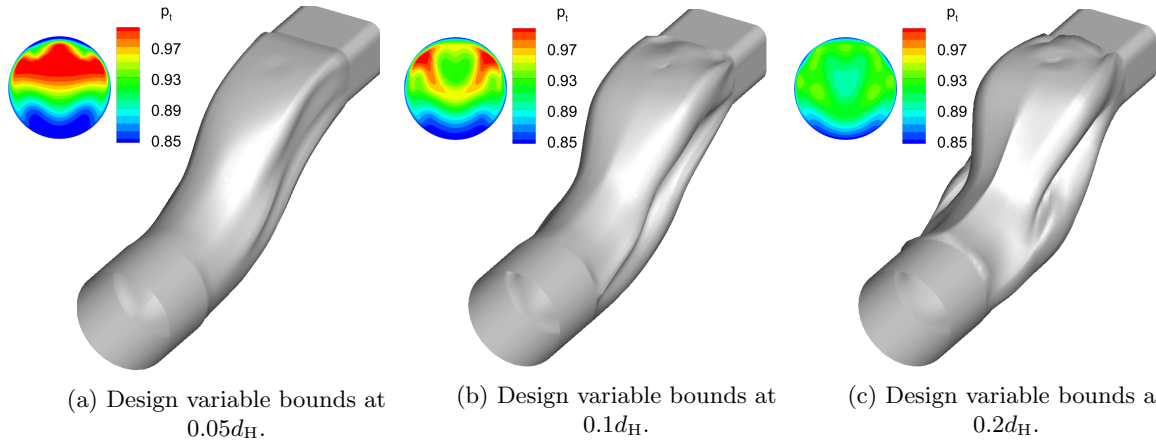


Figure 3.11: Optimized geometry and outlet total pressure for pressure recovery, distortion, and swirl with $\alpha = 0.80$ and $\beta = 0.80$ at cruise and different amounts of geometric freedom.

bottom half. As the design variable bounds are increased, the optimizer is able to better achieve its objective. In Figure 3.11c, the geometrical features are much more pronounced. From its total pressure contour, the distortion appears quite favourable compared to the other two shown. Also, the optimized geometries share some similar geometric features. The trend of the upper surface is to expand at the first bend, then form a bottleneck at the second bend. The bottom surface is also gradually expanded as much as possible.

Despite further improvements in S-duct performance with design variable bounds of $0.2d_H$, the increased geometric freedom led to convergence problems with the optimization algorithm. As the design variable bounds are extended, the bounds will inevitably intersect and encroach on the domains of its neighbouring control points. This allows the possibility for the optimizer to displace a control point past its neighbour, which introduces complications with the mesh movement algorithm. During the mesh movement process, the crossover may cause an area of the control mesh to have a negative Jacobian which indicates that the surface has folded in on itself and triggers a failure. As a result, the optimization with $0.2d_H$ experienced these types of failures in the mesh movement algorithm after about 30 design iterations. While it is possible for SNOPT to recover from an infeasible geometry, the failure does hinder

the optimization progress and may cause it to stall.

Furthermore, real-world manufacturability constraints could also have a considerable impact on the design variable bounds and the realizability of optimized geometries. For these reasons, a bound nominally set to 10% of the hydraulic diameter ($0.1d_H$) is conservatively selected, as it avoids most of the optimization convergence issues, yet is still able to maintain adequate proximity between control points and achieve desirable S-duct performance with a reasonable amount of geometric deformation. Future work could look to increase the design variable bounds to $0.2d_H$ to further investigate the capability of the optimization algorithm and the robustness of the aerodynamic performance with respect to a change in flow conditions, with consideration for the manufacturability of the optimized geometries. Alternatively, to address these concerns additional geometric constraints could be implemented in the future to allow greater freedom for the design variable bounds. Experimental testing of the optimized geometries should also be beneficial for validation and to verify that the optimizer is not going beyond the accuracy of the models used.

Chapter 4

Results

This chapter presents the results for the two composite objective functions specified in Section 3.5.2. First, Pareto fronts are generated for each objective function. Then, a pair of points are selected from each Pareto front for further analysis. Lastly, multi-point optimizations are performed to investigate the robustness of the optimization at off-design points and to explore the potential benefit of single-point S-duct morphing against a multipoint design.

4.1 Optimization with Pressure Recovery, Distortion, and Swirl

4.1.1 Pareto Front Characterization

The Pareto front for the composite objective function with total pressure recovery, distortion, and swirl at the cruise operating condition is presented in Figure 4.1a with boundaries at α values of 0.0 and 1.0 and a β value of 1.0. These boundaries are the three combinations of bi-objective functions resulting from Eq. 3.25. A rough sampling of relatively distributed points was selected to get a general idea of the shape of the Pareto front and how the optimization process behaves with varying relative weights.

The three-dimensional Pareto front shows that the surface is entirely convex and that all three objectives are competing. The trade-off between pressure recovery and distortion is plotted in Figure 4.1b. The green curve, which neglects swirl entirely in the composite objective function due to a fixed α value of 1.0, has an elbow at a β value of 0.92. This means that the desirable region to achieve balanced performance is to place more priority on pressure recovery than distortion. For better visual presentation, the baseline performance is plotted as a red line rather than a point in

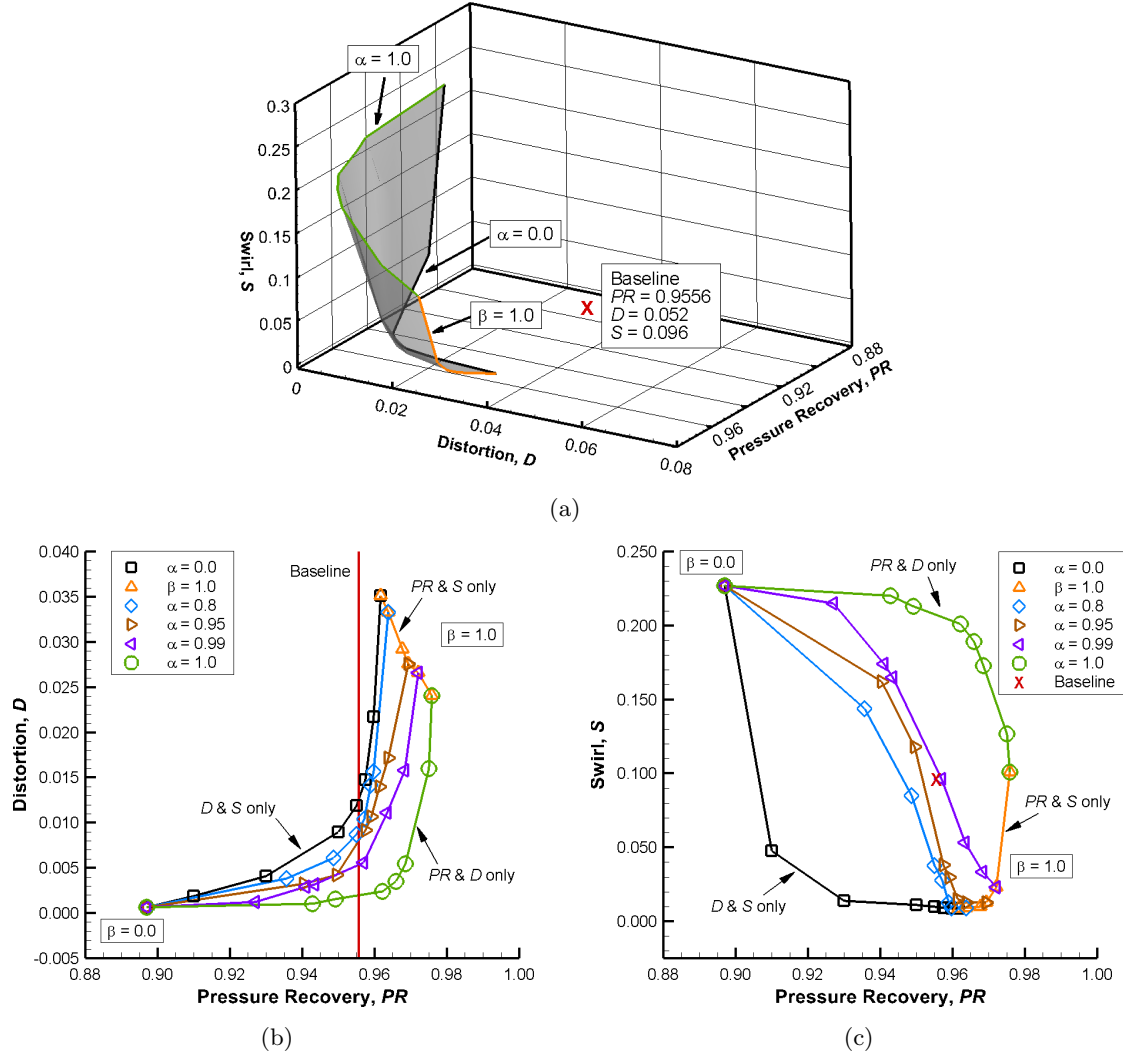


Figure 4.1: Pareto front for the tri-objective function with pressure recovery, distortion, and swirl at cruise.

Figure 4.1b since its distortion far exceeds any result encountered. The other trade-off between pressure recovery and swirl is shown in Figure 4.1c. Here, the elbow of the orange curve is at an α value of 0.95, also indicating that larger weighting on pressure recovery and less on swirl is required in order to be in the desirable range of performance where significant compromises in either objective are not made. Although not shown explicitly, the trade-off between distortion and swirl can be seen from the black curve. With a constant α value of 0.0 throughout this curve, the midpoint is approximately located at a β value of 0.3. Therefore, in order to be located in the range of balanced performance between distortion and swirl, slightly more emphasis should be placed on distortion rather than swirl. In summary, these plots demonstrate that with carefully chosen relative weights, the optimizer is able

Table 4.1: Optimized performance with pressure recovery, distortion, and swirl at cruise and a fan speed of 35,000 RPM.

Objective	Baseline	$\alpha = 1.00, \beta = 0.80$ (PR and D)	$\alpha = 0.95, \beta = 0.90$ (PR, D , and S)
PR	0.956	0.962	0.961
$D \times 10^2$	5.205	0.239	1.360
$S \times 10^2$	9.569	20.07	1.455
L_{var}	0.827	0.061	0.259
ϕ_{var}	0.537	0.026	0.087

to simultaneously improve pressure recovery, distortion, and swirl. However, as one moves away from the elbow region of the front, small improvements in one objective lead to large penalties in the other.

4.1.2 Single-Point Optimization

From Figure 4.1, two pairs of relative weights were selected from the Pareto front for further analysis. With these selected weights, the goal is to investigate how the optimizer manipulates the geometry and the resulting internal flow to achieve its objective at the cruise design point. The first pair is with $\alpha = 1.00$ and $\beta = 0.80$ for Eq. 3.25, which is a bi-objective function between pressure recovery and distortion that neglects swirl. With the same composite objective function formulation, the second pair is with $\alpha = 0.95$ and $\beta = 0.90$, which forms a tri-objective function that includes swirl. Table 4.1 quantitatively summarizes the optimized performance for both results and lists the values of all the objectives considered in this thesis.

Contours of the total pressure, relative blade loading, and relative blade incidence at the outlet are compared in Figure 4.2. In Figure 4.2b, the optimizer was able to lift the low total pressure zone off the bottom surface and towards the outlet centre. The high total pressure region was dispersed circumferentially. Both of these redistributions lead to a reduction of the circumferential distortion of total pressure by 95% in relation to the baseline, while slightly improving pressure recovery by 0.6%. However, since this particular pair of $\alpha = 1.00$ and $\beta = 0.80$ relative weights removed swirl from the objective function, the optimizer was free to manipulate the secondary flows within the S-duct in order to achieve its objective. Although the circumferential variations of blade loading and blade incidence are not included in this objective function, their distributions appear to be favourable. As expected, relative blade loading at the centre is low since the tangential velocity from blade rotation is small and the dominant component of the blade relative velocity comes from the incoming flow. Conversely, for the same reason the relative blade incidence

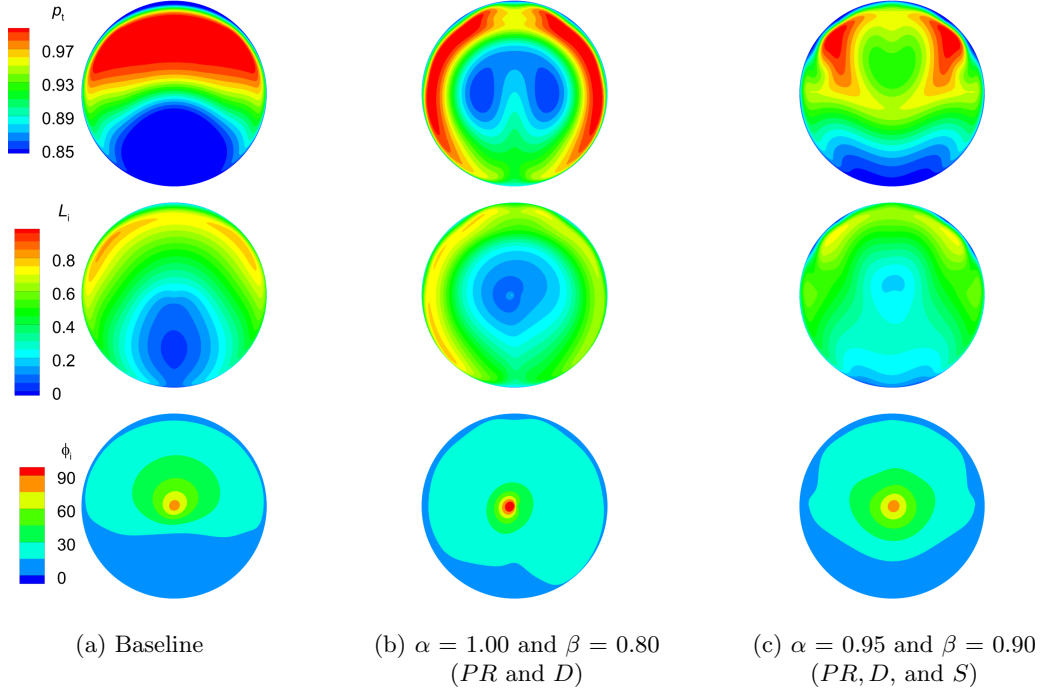


Figure 4.2: Comparison of outlet contours at cruise and a fan speed of 35,000 RPM (PR , D , and S). Total pressure (top), relative blade loading (middle), and relative blade incidence in degrees (bottom).

angle is high at the centre and gradually reduces as the tangential velocity increases with radius. The asymmetry is a result of the addition and cancellation of tangential velocity vectors from the counter-clockwise fan rotation and the symmetric incoming flow. The swirl pair co-rotating with the fan induces a larger relative velocity which increases relative blade loading and reduces relative blade incidence, while the swirl pair counter-rotating with the fan achieves the opposite. Compared to the baseline, the blade load variation is reduced by 93%, with the blade incidence variation down by 95%.

In Figure 4.2c, the optimizer splits the high total pressure zone at the outlet with a lower total pressure core to create more circumferential uniformity. The bottom half of low total pressure has also been flattened in an effort to achieve the same objective of reducing distortion. Here, the distortion has been reduced by 74% compared to the baseline by 0.5%. With swirl now included in the objective function, the optimizer is able to reduce swirl by 85% compared to the baseline. In this case, the relative blade loading and relative blade incidence distributions are quite symmetric. This is due to the minimization of swirl, which removes the tangential component of the velocity vector for the incoming flow and leaves fan rotation as the only contributor

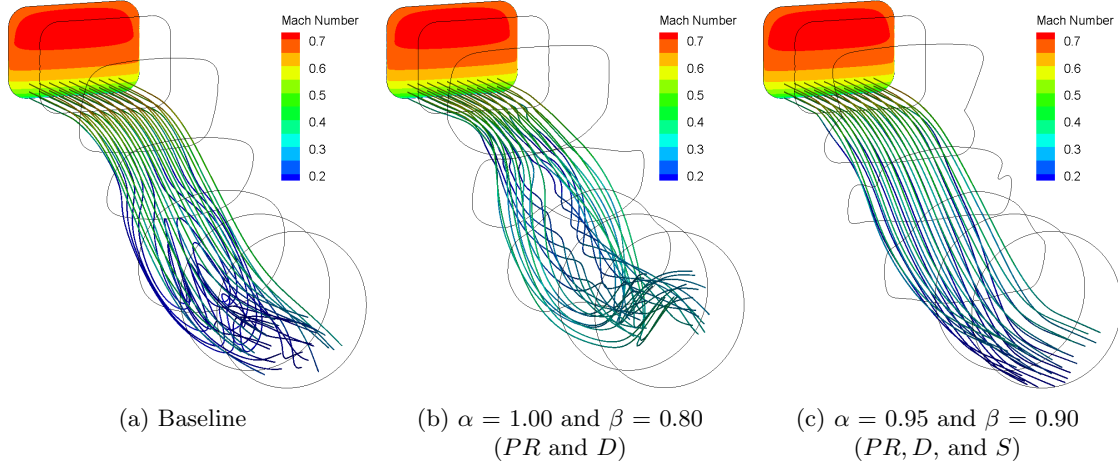


Figure 4.3: Comparison of streamlines at cruise and a fan speed of 35,000 RPM (*PR*, *D*, and *S*).

to tangential velocity. The regions of high and low total pressure correspond well to the regions of high and low relative blade loading. With the low total pressure and relative blade load region present at the bottom surface near the tip, this may still be unfavourable for the fan to accept. This also results in a reduction of the relative blade incidence angle in the lower half of the outlet. The optimized flow indirectly reduces blade load and blade incidence variations by 69% and 84% of the baseline values, respectively.

Figure 4.3b illustrates how swirl is used to lift the low total pressure flow up towards the outlet centre. The increase in vortex strength to redistribute the total pressure doubles the amount of swirl in the flow compared to the baseline. The streamlines of Figure 4.3c demonstrate that the optimizer successfully reduces the incoming swirl to produce a flow field that is relatively axial with little flow angularity.

The optimized shapes are compared against the baseline S-duct in Figure 4.4. In Figure 4.4a, two channels are formed on the bottom surface to accommodate the pair of vortices that shift the low total pressure region towards the centre. The upper surface near the first bend has been expanded to diffuse the flow before being accelerated by the second bend. This results in a more uniform flow velocity at the outlet plane. In Figure 4.4b, the optimizer expands the upper wall at the first bend and forms a centrally-located separation bubble. The bulk flow coming from the top half bypasses this bubble and diverts to the upper corners. It then gets funnelled in a Y-pattern to split the high total pressure zone at the top half of the outlet, losing total pressure in the process, to create more circumferential uniformity. The bottom surface at the first bend has been lowered and the cross-sectional area expanded to reduce the adverse pressure gradient resulting from duct curvature, limit flow separation,

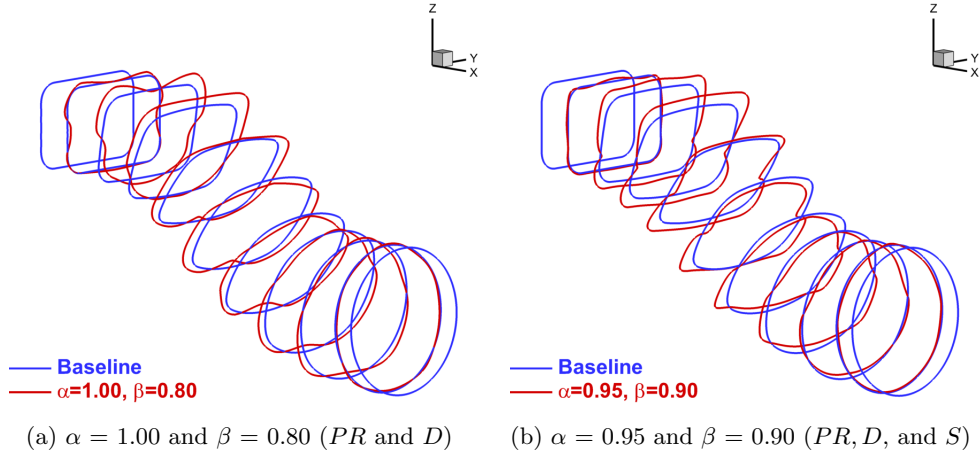


Figure 4.4: Comparison of S-duct geometries at cruise and a fan speed of 35,000 RPM (*PR*, *D*, and *S*).

and better diffuse the flow.

4.1.3 Multipoint Optimization

The current methodology is also extended to multipoint optimizations to investigate the robustness of the design. The goal is to evaluate the potential of S-duct morphing for specific stages of flight against a static multipoint optimized design. To reiterate for clarity, this thesis does not consider how the morphing would be implemented in practice, only its potential benefits with respect to the considered objectives of the S-duct design. The multipoint objective formulations were defined in Section 3.5.3 along with the flow conditions specified in Table 3.2. Two cases are investigated and presented in this section with the composite objective function containing pressure recovery, distortion, and swirl. The first case is with relative weights $\alpha = 1.00$ and $\beta = 0.80$, and the second with $\alpha = 0.95$ and $\beta = 0.90$.

Table 4.2 summarizes the quantitative results for single-point optimizations, meaning different single-point designs optimized for each flight condition that could be achieved through morphing, in the fifth column. Both multipoint optimizations are presented in the sixth and seventh columns respectively. Multipoint 1 with a 2:1:1 ratio corresponds to Eq. 3.27 and multipoint 2 with a 6:1:1 ratio corresponds to Eq. 3.28. The fourth column shows the performance of the cruise-optimized geometry and its performance at descent and climb. The comparisons are made against the baseline performance using $\alpha = 1.00$ and $\beta = 0.80$ that considers pressure recovery and distortion. All five objectives are presented, along with the individual components of the objective function at each operating condition. The percentage increase or decrease from the baseline is also provided in parentheses.

Table 4.2: Performance at multiple operating points optimizing with $\alpha = 1.00$ and $\beta = 0.80$ (PR and D).

Condition	Objective	Baseline	Cruise-Optimized	Single-point Morphing	Multipoint 1 (2:1:1)	Multipoint 2 (6:1:1)
Cruise	PR	0.956	0.962 (+0.6%)	0.951 (-0.5%)	0.960 (+0.4%)	
	$D \times 10^2$	5.205	0.239 (-95%)	0.244 (-95%)	0.235 (-96%)	
	$S \times 10^2$	9.570	20.07 (+110%)	21.54 (+125%)	20.71 (+116%)	
	L_{var}	0.827	0.061 (-93%)	0.066 (-92%)	0.066 (-92%)	
	ϕ_{var}	0.537	0.026 (-95%)	0.027 (-95%)	0.029 (-95%)	
	$\mathcal{J}_{1, \text{cruise}}$	1.000	0.804	0.814	0.806	
Descent	PR	0.963	0.974 (+1.1%)	0.968 (+0.5%)	0.966 (+0.3%)	0.972 (+0.9%)
	$D \times 10^2$	3.696	0.466 (-87%)	0.167 (-95%)	0.199 (-95%)	0.351 (-91%)
	$S \times 10^2$	10.24	17.42 (+70%)	20.36 (+99%)	20.63 (+101%)	18.28 (+79%)
	L_{var}	0.620	0.078 (-87%)	0.047 (-92%)	0.054 (-91%)	0.070 (-89%)
	ϕ_{var}	0.588	0.040 (-93%)	0.031 (-95%)	0.027 (-95%)	0.034 (-94%)
	$\mathcal{J}_{1, \text{descent}}$	1.000	0.818	0.807	0.810	0.813
Climb	PR	0.992	0.994 (+0.2%)	0.992 (0%)	0.992 (0%)	0.994 (+0.2%)
	$D \times 10^2$	0.203	0.050 (-75%)	0.014 (-93%)	0.018 (-91%)	0.043 (-79%)
	$S \times 10^2$	7.390	12.82 (+73%)	16.15 (+119%)	15.17 (+105%)	13.20 (+79%)
	L_{var}	0.178	0.035 (-80%)	0.017 (-90%)	0.021 (-88%)	0.033 (-81%)
	ϕ_{var}	0.085	0.017 (-80%)	0.004 (-95%)	0.007 (-92%)	0.015 (-82%)
	$\mathcal{J}_{1, \text{climb}}$	1.000	0.848	0.815	0.818	0.841

The general trends identified in Section 4.1.2 are consistent when extended to multiple operating conditions. With the specified weighting, the optimizer is able to maintain or slightly improve pressure recovery and significantly reduce distortion as intended. The exception here is the pressure recovery at multipoint 1, which is lower than the baseline. With swirl excluded from the objective function, the swirl generally doubles at every operating condition. This confirms that the optimizer is increasing the swirl as a method to reduce distortion and shift the low total pressure region toward the outlet centre. As expected, the single-point morphing objective function values outperform the multipoint values, since the optimizer focuses on one condition specifically; however, the single-point morphing performance gain over the multipoint optimizations is relatively small in general. In this case, between multipoint 1 and multipoint 2, placing more priority on the cruise condition with a 6:1:1 ratio does provide better cruise performance at the cost of reduced performance at descent and climb compared to multipoint 1. When descent and climb conditions are not considered for optimization as in the cruise-optimized geometry, the resulting S-duct provides better pressure recovery at descent and climb with a small trade-off in distortion compared to the single-point and multipoint cases. Although not directly accounted for in the objective function, blade load and blade incidence variation are

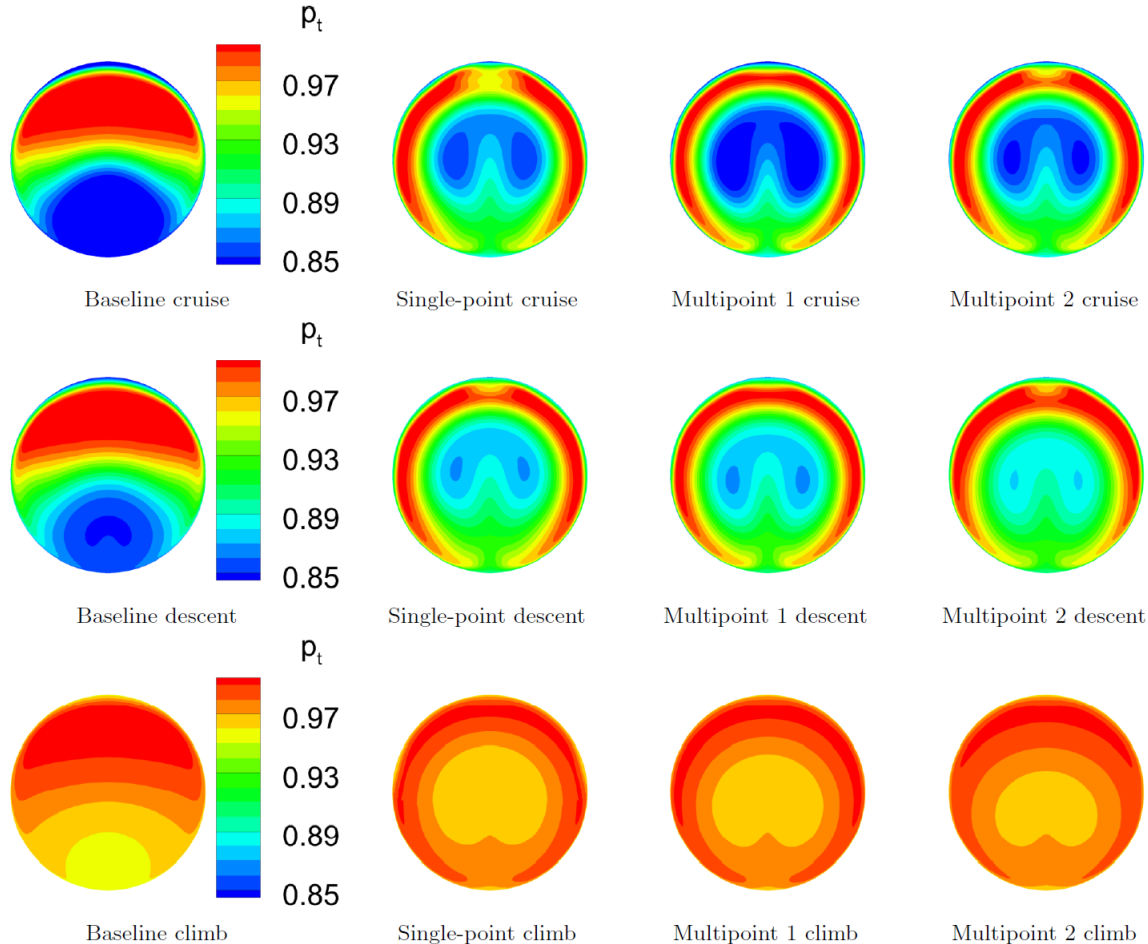


Figure 4.5: Outlet total pressure contours optimizing with $\alpha = 1.00$, $\beta = 0.80$ (PR and D).

generally much lower than the baseline across all three operating conditions.

A comparison of the outlet total pressure is shown in Figure 4.5. The contours are consistent at every operating condition with the region of low total pressure located near the centre and the high total pressure region being circumferentially redistributed. The low total pressure region is centred very well in the single-point column which corresponds to the lowest amount of circumferential distortion. The multipoint columns demonstrate that as less weighting is placed on descent and climb, the low total pressure region becomes increasingly off-centred. As one would expect, this shows the trades between different flight conditions and their dependence on the multipoint weightings.

Comparing the single and multipoint columns for this particular set of weights, there is not a significant benefit for single-point morphing since the total pressure distributions are quite similar and both multi-point optimized geometries appear to mitigate distortion fairly well at every operating condition. In reference to climb, the

Table 4.3: Performance at multiple operating points optimizing with $\alpha = 0.95$ and $\beta = 0.90$ (PR , D , and S).

Condition	Objective	Baseline	Cruise-Optimized	Single-point Morphing	Multipoint 1 (2:1:1)	Multipoint 2 (6:1:1)
Cruise	PR	0.956	0.961 (+0.5%)	0.960 (+0.4%)	0.961 (+0.5%)	
	$D \times 10^2$	5.205	1.360 (-74%)	1.348 (-74%)	1.355 (-74%)	
	$S \times 10^2$	9.569	1.455 (-85%)	1.701 (-82%)	1.468 (-85%)	
	L_{var}	0.827	0.259 (-69%)	0.249 (-70%)	0.249 (-70%)	
	ϕ_{var}	0.537	0.087 (-84%)	0.082 (-85%)	0.082 (-85%)	
	$\mathcal{J}_{1, \text{cruise}}$	1.000	0.882	0.884	0.883	
Descent	PR	0.963	0.969 (+0.6%)	0.969 (+0.6%)	0.968 (+0.5%)	0.969 (+0.6%)
	$D \times 10^2$	3.696	1.322 (-64%)	1.288 (-65%)	1.303 (-65%)	1.316 (-64%)
	$S \times 10^2$	10.24	1.257 (-88%)	1.316 (-87%)	1.454 (-86%)	1.237 (-88%)
	L_{var}	0.620	0.259 (-58%)	0.243 (-61%)	0.247 (-60%)	0.248 (-60%)
	ϕ_{var}	0.588	0.144 (-76%)	0.129 (-78%)	0.133 (-77%)	0.135 (-77%)
	$\mathcal{J}_{1, \text{descent}}$	1.000	0.891	0.890	0.892	0.891
Climb	PR	0.992	0.993 (+0.1%)	0.992 (0%)	0.993 (+0.1%)	0.993 (+0.1%)
	$D \times 10^2$	0.203	0.122 (-40%)	0.071 (-65%)	0.129 (-36%)	0.122 (-40%)
	$S \times 10^2$	7.390	5.267 (-29%)	1.231 (-83%)	4.660 (-37%)	5.183 (-30%)
	L_{var}	0.178	0.073 (-59%)	0.065 (-63%)	0.094 (-47%)	0.092 (-48%)
	ϕ_{var}	0.085	0.027 (-68%)	0.023 (-73%)	0.045 (-47%)	0.043 (-49%)
	$\mathcal{J}_{1, \text{climb}}$	1.000	0.946	0.897	0.946	0.946

multipoint 1 contour is similar in size and shape to single-point. A small trade-off in climb could be made in multipoint 2 if better total pressure recovery is desired at cruise.

Next, Table 4.3 presents the results for $\alpha = 0.95$ and $\beta = 0.90$ to maximize pressure recovery and minimize distortion and swirl simultaneously. From the table, it is evident that the optimizer was able to improve all three objectives at every operating condition for both single-point and multipoint. The single-point objective function values at cruise and descent are superior to both multipoint values, but only slightly. The single-point climb values for distortion and swirl are reduced even further by approximately a factor of two compared to the cruise-optimized geometry, multipoint 1, and multipoint 2. Unlike the previous multipoint 1 and multipoint 2 results for $\alpha = 1.00$ and $\beta = 0.80$, the discrepancy between the performance at multipoint 1 and multipoint 2 is much smaller here. This may suggest that the geometry is insensitive to the multipoint weighting between operating conditions once swirl is included in the objective function. It can also be noted that blade load and blade incidence variation were reduced by generally similar percentages as the distortion.

Observing the outlet total pressure contours in Figure 4.6, the flow features appear

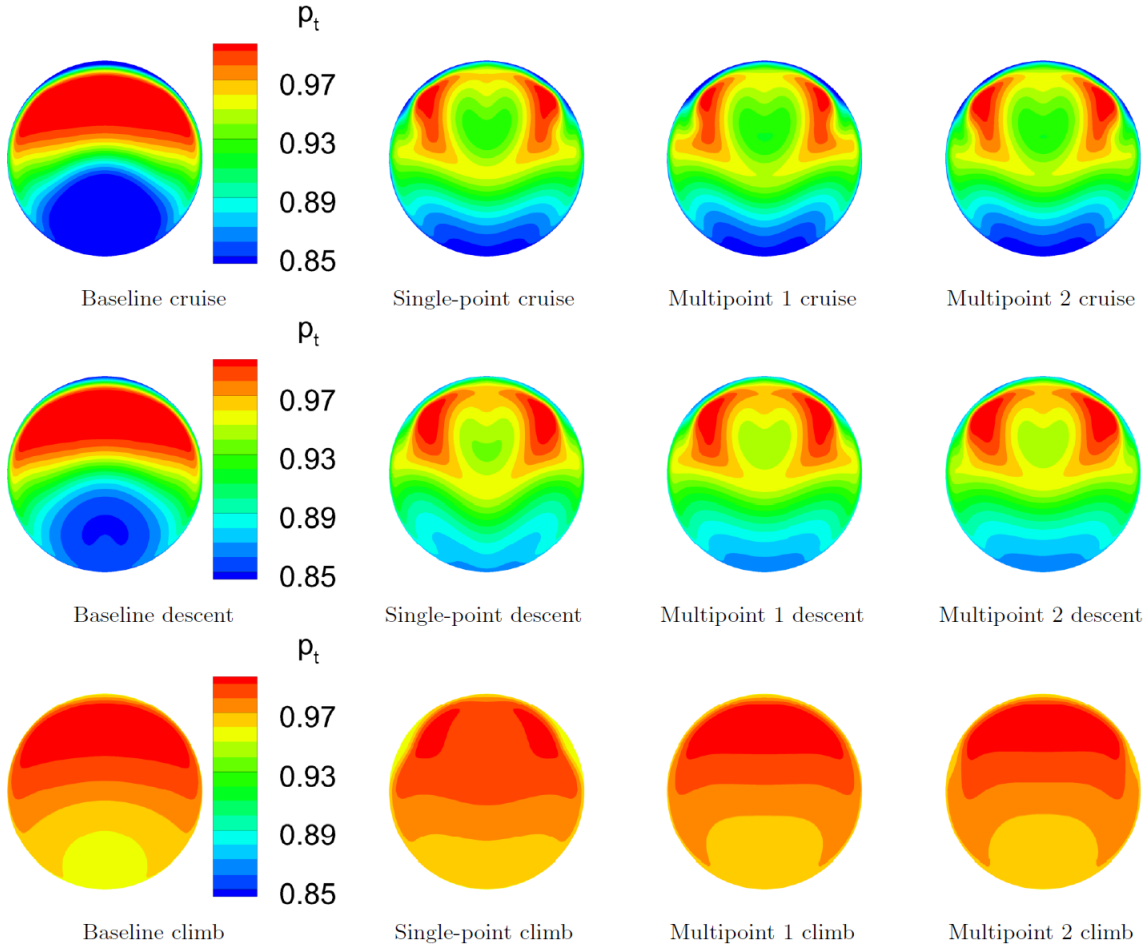


Figure 4.6: Outlet total pressure contours optimizing with $\alpha = 0.95$, $\beta = 0.90$ (PR , D , and S).

to be quite similar and consistent with the features identified in Section 4.1.2. At cruise and descent, the high total pressure region in the top half is bisected with a core of lower pressure and the low total pressure region is flattened. This type of flow redistribution also appears during climb conditions but is not clear due to contour scaling. Therefore, this particular pair of values for α and β weights also show the lack of benefit for single-point morphing. At every operating condition, the presence of the low total pressure region remains in the lower portion of the outlet near the fan blade tip. This could potentially risk exposing the fan to unfavourable conditions that outweigh the concerns of minimizing swirl in the flow. It is difficult to determine which aspect is more detrimental to fan performance and further work is required to incorporate a method to evaluate fan performance.

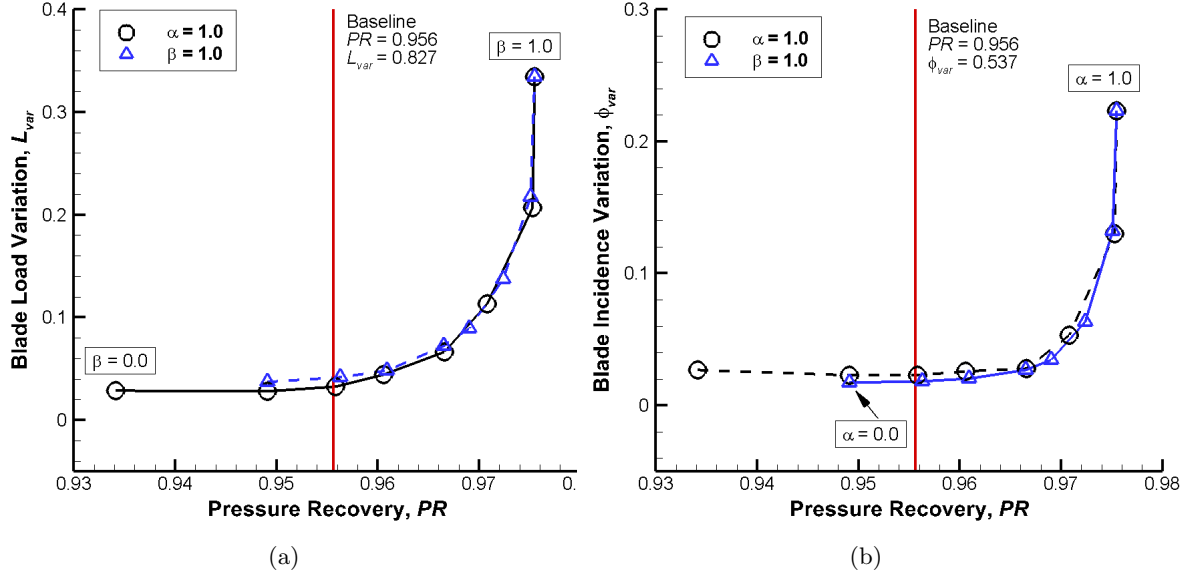


Figure 4.7: Pareto fronts for the tri-objective function with pressure recovery, blade load variation, and blade incidence variation at cruise and a fan speed of 35,000 RPM. Dashed lines indicate the performance of the other Pareto curve superimposed in the current domain.

4.2 Optimization with Pressure Recovery and Blade Variation Parameters

4.2.1 Pareto Front Characterization

In consideration of total pressure recovery, blade load variation, and blade incidence variation in the composite objective function, Figure 4.7 plots the Pareto curves. Again, the baseline geometry is represented with a red line rather than a point, as its variation in blade loading and blade incidence exceeds the axis range. Here, a three-dimensional view is not necessary since the Pareto curve for pressure recovery and blade load variation, which is the black line with $\alpha = 1.00$ and varying β values, is nearly coincident to the Pareto curve for pressure recovery and blade incidence variation, which is the blue line with $\beta = 1.00$ and varying α values. Hence, these curves adequately demonstrate the convex trade-off between the objectives considered and no further combinations of relative weights are required. In Figure 4.7a, the optimizer was able to considerably reduce the blade load variation across the entire range of β values. Values larger than $\beta = 0.95$, the third black circle from the right, or smaller than $\beta = 0.75$, the fourth black circle from the left, lead to diminishing returns in one objective with large penalties in the other. Thus, β values ranging from 0.75 to 0.95 are of interest since they provide substantial reduction in blade load variation while outperforming the baseline pressure recovery. Similarly, in Figure 4.7b

Table 4.4: Optimized performance with pressure recovery, blade load variation, and blade incidence variation at cruise and a fan speed of 35,000 RPM.

Objective	Baseline	$\alpha = 1.00, \beta = 0.95$ (PR and L_{var})	$\alpha = 0.90, \beta = 1.00$ (PR and ϕ_{var})
PR	0.956	0.971	0.969
$D \times 10^2$	5.205	1.015	0.697
$S \times 10^2$	9.569	14.64	16.74
L_{var}	0.827	0.113	0.089
ϕ_{var}	0.537	0.053	0.035

the blade incidence variation is considerably reduced for all α values compared to the baseline. Values larger than $\alpha = 0.95$, third blue triangle from the right, or smaller than $\alpha = 0.90$, fourth blue triangle from the right, lead to diminishing returns in one objective with large penalties in the other. Thus, α values ranging from 0.90 to 0.95 are of interest since they provide substantial reduction in blade incidence variation while outperforming the baseline pressure recovery.

4.2.2 Single-Point Optimization

From the Pareto curves in Figure 4.7, two pairs of relative weights were selected. For the second composite objective function from Eq. 3.26, the first pair is with $\alpha = 1.00$ and $\beta = 0.95$, which is a bi-objective function between pressure recovery and blade load variation. The second pair is with $\alpha = 0.90$ and $\beta = 1.00$, which is another bi-objective function that considers pressure recovery and blade incidence variation. The optimized performance values are listed in Table 4.4.

Contours of the total pressure, relative blade loading, and relative blade incidence at the outlet are compared in Figure 4.8. It is immediately evident that all three pairs of contours look similar and resemble those from Figure 4.2b. The distributions of relative blade loading and relative blade incidence appear to be favourable. Targeting pressure recovery and blade load variation with $\alpha = 1.00$ and $\beta = 0.95$, the optimizer reduces the baseline blade load variation by 87%. The blade incidence variation and distortion are reduced by 90% and 85% respectively, relative to the baseline. Using relative weights $\alpha = 0.90$ and $\beta = 1.00$, the blade incidence variation is reduced by 93% compared to the baseline. The blade load variation and distortion are reduced by 89% and 87% respectively, relative to the baseline.

From the visualization of streamlines, Figures 4.9b and 4.9c demonstrate that swirl is present at the fan face. The swirl values for both cases are roughly 1.5 times larger than the baseline. The vortices are also more concentrated and tighter compared to those observed in Figure 4.3b.

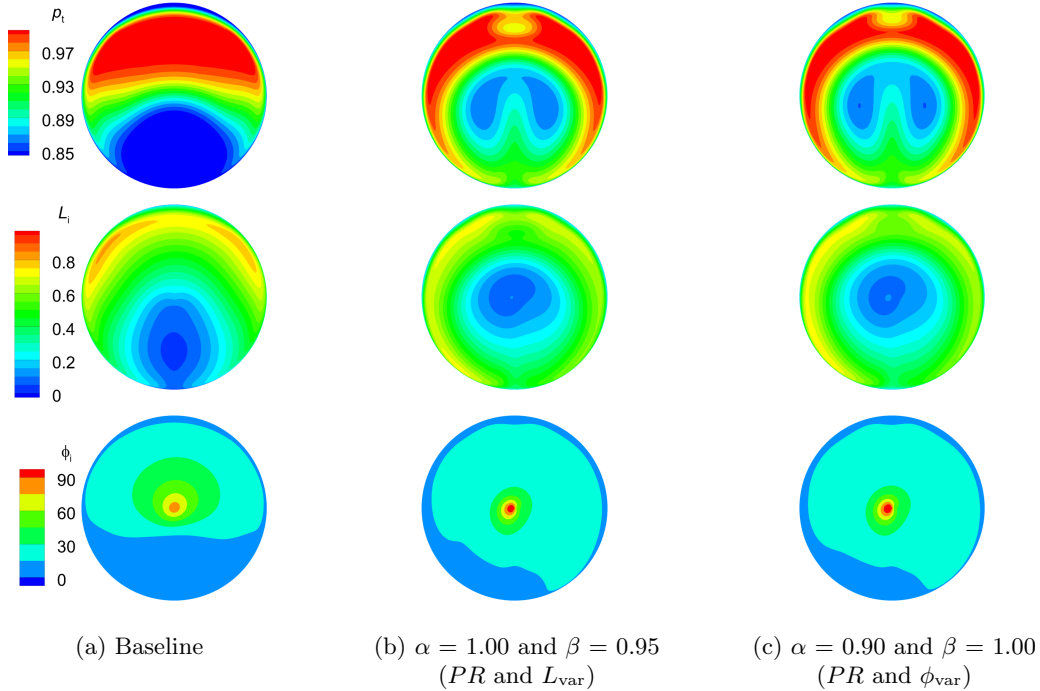


Figure 4.8: Comparison of outlet contours at cruise and a fan speed of 35,000 RPM (PR , L_{var} , and ϕ_{var}). Total pressure (top), relative blade loading (middle), and relative blade incidence in degrees (bottom).

The optimized shapes are compared against the baseline S-duct in Figure 4.10. Much like their outlet contours, the optimized geometries from Figures 4.10a and 4.10b are similar in shape to Figure 4.4a, indicating that the optimizer is using the same flow features to achieve its objective.

4.2.3 Multipoint Optimization

Progressing to multipoint optimizations, Table 4.5 with $\alpha = 0.90$ and $\beta = 1.00$ presents a quantitative summary for the composite objective function containing pressure recovery and blade incidence variation. The other multipoint runs with $\alpha = 1.00$ and $\beta = 0.95$ are not shown since the same conclusions can be drawn from either set of results.

Once again, the optimizer was able to significantly reduce the blade incidence variation while maintaining or improving the pressure recovery of the baseline. The blade load variation was not included in the objective function but was reduced by nearly the same percentage as the blade incidence variation. Distortion and swirl were also not optimized for, but the distortion was reduced as well. On the other hand, the swirl increased to around one and a half times that of the baseline. This increase was also observed in Section 4.1.3 when optimizing for pressure recovery

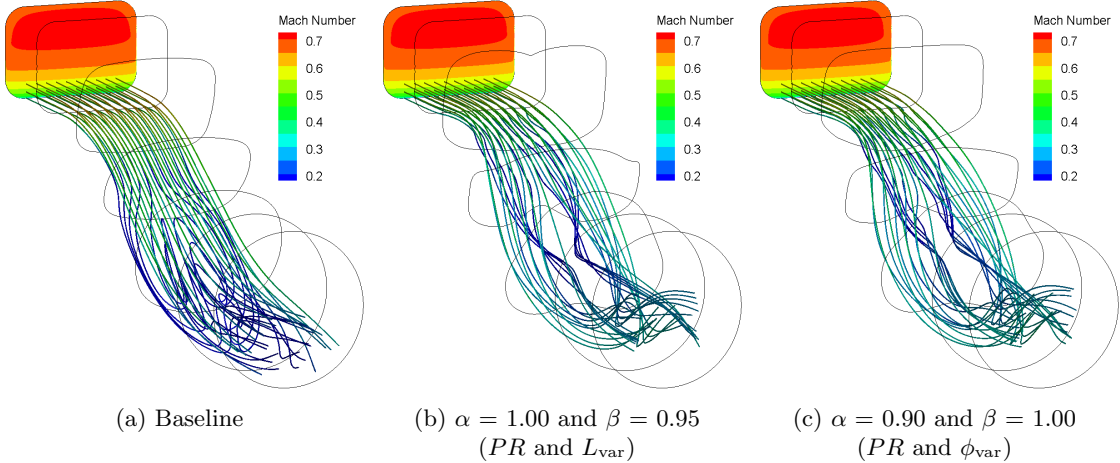


Figure 4.9: Comparison of streamlines at cruise and a fan speed of 35,000 RPM (PR , L_{var} , and ϕ_{var}).

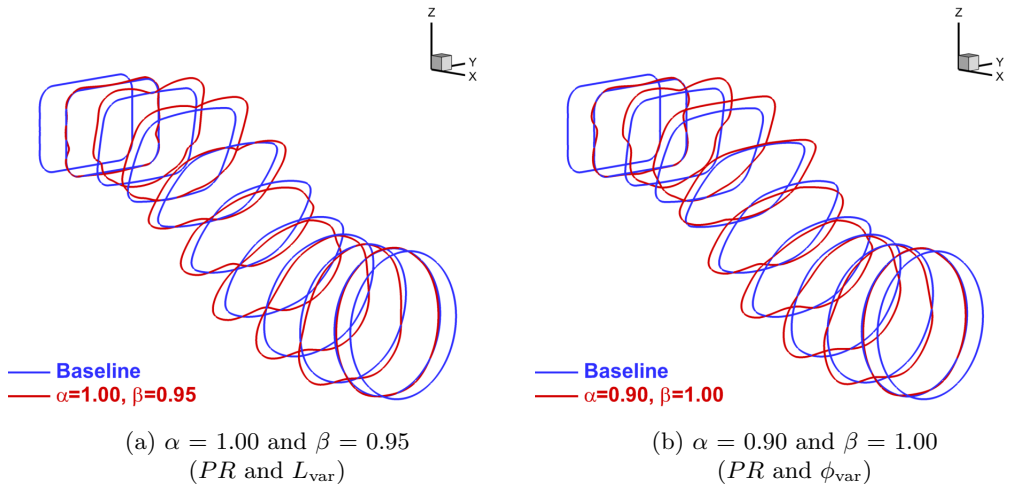


Figure 4.10: Comparison of S-duct geometries at cruise and a fan speed of 35,000 RPM (PR , L_{var} , and ϕ_{var}).

and distortion and raises an important question about the impact of swirl on fan performance and efficiency. Here, the single-point objective function values are only slightly better than the multipoint values at all three operating conditions. The cruise-optimized geometry at descent and climb have better pressure recoveries with a small trade-off in blade incidence variation compared to single-point and multipoint. Furthermore, there is not a large difference between the performance at multipoint 1 and multipoint 2, indicating that the greater prioritization of cruise in multipoint 2 did not improve cruise performance by a significant margin.

The outlet total pressure contours in Figure 4.11 demonstrate a similar flow field to that of Figure 4.5, where the high total pressure region is pulled around the outer circumference and the low total pressure region is lifted from the bottom surface

Table 4.5: Performance at multiple operating points optimizing with $\alpha = 0.90$ and $\beta = 1.00$ (PR and ϕ_{var}).

Condition	Objective	Baseline	Cruise-Optimized	Single-point Morphing	Multipoint 1 (2:1:1)	Multipoint 2 (6:1:1)
Cruise	PR	0.956	0.969 (+1.3%)	0.965 (+0.9%)	0.966 (+1.0%)	
	L_{var}	0.827	0.089 (-89%)	0.109 (-87%)	0.115 (-86%)	
	ϕ_{var}	0.537	0.035 (-93%)	0.041 (-92%)	0.045 (-92%)	
	$D \times 10^2$	5.205	0.697 (-87%)	0.999 (-81%)	1.057 (-80%)	
	$S \times 10^2$	9.569	16.74 (+75%)	16.31 (+70%)	15.66 (+64%)	
	$\mathcal{J}_{2, \text{cruise}}$	1.000	0.895	0.899	0.898	
Descent	PR	0.963	0.977 (+1.4%)	0.974 (+1.1%)	0.974 (+1.1%)	0.975 (+1.2%)
	L_{var}	0.620	0.105 (-83%)	0.063 (-90%)	0.081 (-87%)	0.091 (-85%)
	ϕ_{var}	0.588	0.069 (-88%)	0.034 (-94%)	0.048 (-92%)	0.055 (-91%)
	$D \times 10^2$	3.696	0.845 (-77%)	0.445 (-88%)	0.688 (-81%)	0.765 (-79%)
	$S \times 10^2$	10.24	14.74 (+44%)	16.97 (+66%)	16.04 (+57%)	15.30 (+49%)
	$\mathcal{J}_{2, \text{descent}}$	1.000	0.900	0.897	0.899	0.899
Climb	PR	0.992	0.995 (+0.3%)	0.992 (0%)	0.994 (+0.2%)	0.994 (+0.2%)
	L_{var}	0.178	0.034 (-81%)	0.011 (-94%)	0.021 (-88%)	0.025 (-86%)
	ϕ_{var}	0.085	0.017 (-80%)	0.006 (-93%)	0.008 (-91%)	0.012 (-86%)
	$D \times 10^2$	0.203	0.055 (-73%)	0.017 (-92%)	0.035 (-83%)	0.043 (-79%)
	$S \times 10^2$	7.390	11.95 (+62%)	16.99 (+130%)	13.82 (+87%)	12.85 (+74%)
	$\mathcal{J}_{2, \text{climb}}$	1.000	0.918	0.904	0.908	0.912

and placed near the outlet centre. As such, the benefit of morphing is relatively small. A notable difference however is that the low total pressure region is divided into two distinct lobes on each side of the central symmetry plane. This once again demonstrates the trade-off between different flight conditions, in both on- and off-design points as well as the reliance on the multipoint weights to determine those trade-offs.

4.3 Presence of Multimodality

Evidence of multimodality with this aerodynamic shape optimization problem has been observed throughout the optimizations. This was particularly challenging during the process of generating Pareto fronts for both composite objective functions, but several instances of multimodality were also encountered during the multipoint optimizations. Since optimization runs are typically initiated from the baseline geometry, coupled with the fact that a gradient-based optimization algorithm is employed, in some cases this may lead to multiple local minima. In most instances, it is generally difficult to distinguish whether the optimizer has found a local or a global optimum. However, while generating the Pareto front, an inferior local optimum can be clearly

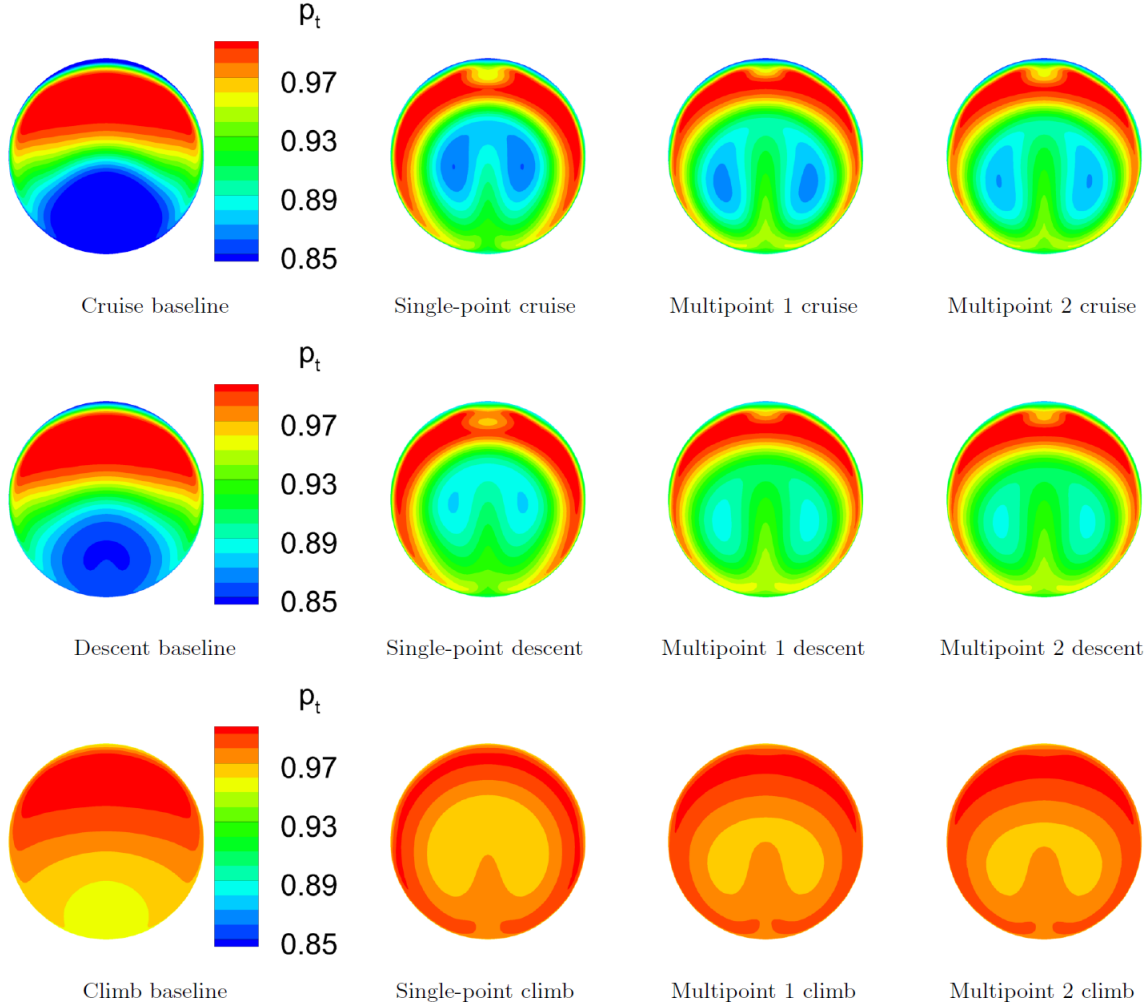


Figure 4.11: Outlet total pressure contours optimizing with $\alpha = 0.90$, $\beta = 1.00$ (PR and ϕ_{var}).

identified if it does not lie on the Pareto front. In order to increase the probability of finding a set of points that are either located on the Pareto front or consistently high quality local optima (i.e. the “superior” local optimum), an optimization can be initiated from another optimized geometry that lies on the Pareto front if an inferior local optimum is encountered. Another alternative approach to addressing multimodality is the gradient-based multistart approach of Chernukhin and Zingg [9, 60]. Although this approach is efficient, it is nevertheless expensive, and it was not used here. Instead, precautions were taken to avoid suboptimal local minima, as described above, and any anomalous results have been carefully revisited with a suitable initial geometry.

An example of multimodality is discussed in this section using the composite objective function with pressure recovery and blade incidence variation with $\alpha = 0.90$, $\beta = 1.00$. In Table 4.6, the optimizer found a solution with a better objective function

Table 4.6: Cruise optimized performance showing multimodality with $\alpha = 0.90$, $\beta = 1.00$ (PR and ϕ_{var}).

Initial Condition	Objective Function	Pressure Recovery	Blade Incidence Variation
Optimized from baseline	0.8997	0.9666	0.0526
Optimized from $\alpha = 0.95$ (PR and ϕ_{var})	0.8948	0.9690	0.0345

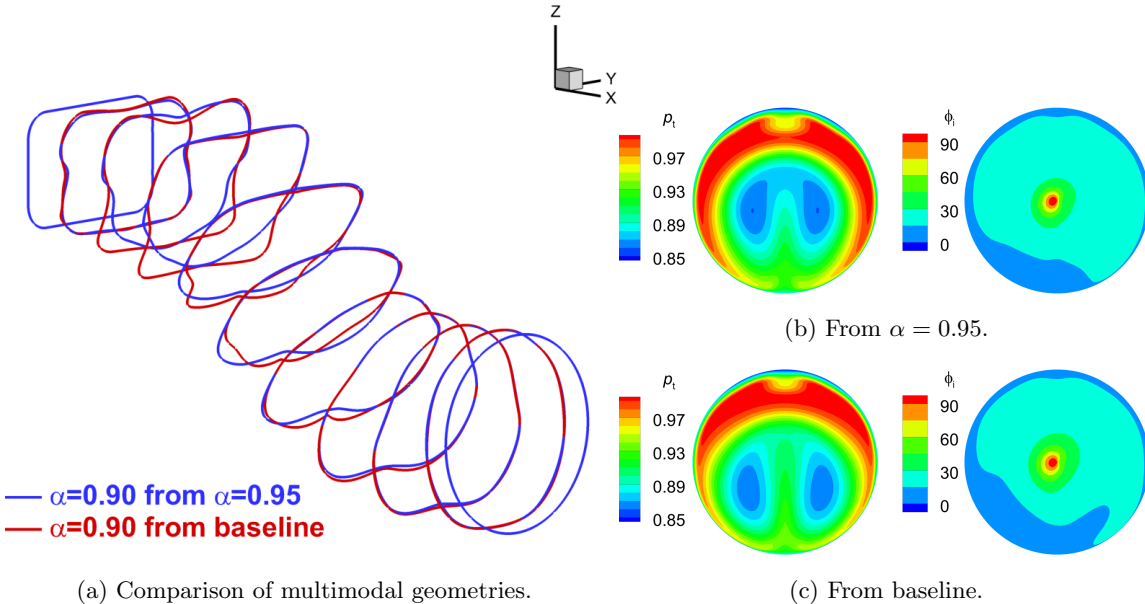


Figure 4.12: Evidence of multimodality.

value optimizing from another point on the Pareto curve than optimizing from the baseline. This initial point is $\alpha = 0.95$, $\beta = 1.00$, the third blue triangle from the right of Figure 4.7b. The fourth blue triangle from the right is $\alpha = 0.90$, $\beta = 1.00$, optimized from the third blue triangle. Furthermore, plotting the local minimum that was found by optimizing from the baseline places that point slightly above and to the left of the fourth blue triangle. Since this point is not located on the curve, it is not Pareto optimal, meaning that this point is dominated by another point on the Pareto curve that is better in both pressure recovery and blade incidence variation.

Looking closer at the results in Figure 4.12a, the difference in geometries is apparent in the lower surface of the first bend. The inferior geometry went towards a path of increasing the area to diffuse the flow whereas the superior geometry constricted the lower surface. For both cases, the KKT residual for optimality was reduced by nearly two orders of magnitude. Furthermore, restarting the optimization from both geometries did not significantly improve the objective function or the optimality, nor was the optimizer able to recover and converge to the better local minimum.

Figures 4.12b and 4.12c demonstrate the difference in total pressure and relative

blade incidence at the outlet plane, particularly in the bottom section. The low total pressure region is much more centred by the better local optimum, with the high total pressure region extending lower around the circumference. Also, the low total pressure regions of the inferior local optimum are distinctly split in two. This has further implications for the relative blade incidence, as the two separate lobes in the bottom section are approximately in the same location as the spike in the bottom right half of the outlet, indicating a region of lower incidence angle.

Chapter 5

Conclusions and Recommendations

5.1 Conclusions

The aerodynamic shape optimization framework Jetstream has demonstrated its capability in handling the multi-objective nature of intake design for a BLI S-duct. The focus of the optimizations was on the aerodynamic performance defined at the fan interface plane where two composite objective functions were investigated. One combines pressure recovery, distortion, and swirl, the other pressure recovery, blade load variation, and blade incidence variation. Pareto fronts are generated with the weighted-sum method by varying the weights of each objective to demonstrate the trade-offs between competing objectives. Both single-point and multipoint optimizations are performed, considering cruise, descent, and climb conditions to assess the potential benefits of a morphing S-duct. From the results, the following conclusions can be drawn:

- The Pareto fronts demonstrate that pressure recovery and fan-face distortion are competing objectives. Distortion and swirl at the fan interface plane also compete. At the expense of a high amount of swirl, distortion can be significantly reduced. Reducing both distortion and swirl at the fan face presents more of a challenge. It is difficult to determine if swirl can be ignored; hence it is important to gain a better understanding of the importance of fan-face swirl on fan efficiency.
- To improve performance in terms of fan-face distortion, blade load variation, or blade incidence variation, the optimizer increases the swirl in the flow to shift the low total pressure region from the bottom towards the centre and circumferentially redistributes the high total pressure region. If swirl performance cannot be ignored, the low total pressure region is reduced in size but remains in the

bottom portion of the fan interface plane near the fan tip.

- The results indicate that a single geometry determined from a multipoint optimization can provide good aerodynamic performance at multiple operating points for the range of conditions considered in this thesis. This suggests that the benefits of S-duct morphing may be small for this application.
- Multimodality was observed with this aerodynamic shape optimization problem. A gradient-based optimization algorithm was used for its computational efficiency; however, this method may be susceptible to finding multiple local minima which are not Pareto optimal. Any anomalous optimization results were carefully revisited with alternate initial geometries to locate the highest quality local optimum.

5.2 Recommendations

For future work, the following candidates are recommended for consideration:

- **Additional geometric freedom**

The expansion of FFD bounding box constraints can be explored to investigate the benefit in achievable aerodynamic performance at the expense of the stability and convergence of the optimization algorithm as well as manufacturability constraints. As the box constraints are expanded, additional geometric constraints could be developed to alleviate some of the problems associated with the mesh movement algorithm. In addition, allowing for an asymmetric S-duct could achieve better performance in blade load or blade incidence variation that account for the direction of fan rotation.

- **Experimental validation**

Although the flow solver was validated for the baseline configuration at cruise, it would be beneficial to experimentally validate the performance of any one of the geometries optimized for BLI. This would provide confidence in the flow solver predictions and that the optimizer correctly interprets and manipulates the flow physics to improve the design.

- **Multimodality**

Multimodality is a problem observed in most aerodynamic shape optimization problems. The application of the gradient-based multistart algorithm developed by Chernukhin and Zingg [9] would provide more extensive coverage of the design

space with a range of initial geometries and additional confidence that the global minimum has been found.

- **Fan predictive capability**

Additional work towards a predictive capability for fan performance under inlet distortion is also important to understand the relative importance of swirl on fan efficiency. The body force model [43, 69] is a RANS-based formulation to simulate a propulsor without physically modeling the fan blades and is capable of capturing intake-fan interactions. In the absence of simulating rotating turbomachinery, this significantly reduces the computational cost, in addition to loosening the requirement for a highly refined mesh. This model could provide an initial estimate of the fan efficiency penalty for BLI systems. The model also presents an opportunity to develop a coupled fan blade-intake optimization framework.

- **Analysis of a BWB configuration with a BLI S-duct installation**

As this work was conducted with a purely internal flow domain, a logical progression is to extend the computational domain to include both internal and external flows. A starting point can be to investigate a single BLI S-duct installation on a regional-class blended wing body configuration.

References

- [1] “A Methodology for Assessing Inlet Swirl Distortion,” SAE International, SAE S-16 Turbine Engine Inlet Flow Distortion Committee, AIR5686, Tech. Rep., 2017.
- [2] Arntz, A. and Atinault, O., “Exergy-Based Performance Assessment of a Blended Wing-Body with Boundary-Layer Ingestion,” *AIAA Journal*, vol. 53, no. 12, pp. 3766–3776, 2015.
- [3] Arntz, A., Atinault, O., and Merlen, A., “Exergy-Based Formulation for Aircraft Aeropropulsive Performance Assessment: Theoretical Development,” *AIAA Journal*, vol. 53, no. 6, pp. 1627–1639, 2015.
- [4] Arntz, A. and Hue, D., “Exergy-Based Performance Assessment of the NASA Common Research Model,” *AIAA Journal*, vol. 54, no. 1, pp. 88–100, 2016.
- [5] Asghar, A., Stowe, R. A., Allan, W. D. E., and Alexander, D., “Performance Evaluation of an S-Duct Diffuser of a Flight-Vehicle Inlet in High-Subsonic Flow,” in *Proceedings of ASME Turbo Expo 2015: Turbine Technical Conference and Exposition*, June 2015, GT2015-43740.
- [6] Ball, W. H., “Tests of Wall Suction and Blowing in Highly Offset Diffusers,” *Journal of Aircraft*, vol. 22, no. 3, pp. 161–167, 1985.
- [7] Betz, A., *Introduction to the Theory of Flow Machines*, 1st ed. New York: Pergamon, 1966, pp. 215, 217.
- [8] Carlson, J.-R., “Inflow/Outflow Boundary Conditions with Application to FUN3D,” NASA Langley Research Center, TM-2011-217181, Tech. Rep., 2011.
- [9] Chernukhin, O. and Zingg, D. W., “Multimodality and Global Optimization in Aerodynamic Design,” *AIAA Journal*, vol. 51, no. 6, pp. 1342–1354, 2013.
- [10] Chiereghin, N., Guglielmi, L., Savill, A. M., Kipouros, T., Manca, E., Rigobello, A., Barison, M., and Benini, E., “Shape Optimization of a Curved Duct with Free Form Deformations,” in *23rd AIAA Computational Fluid Dynamics Conference*, June 2017, AIAA 2017-4144.
- [11] Cousins, W. T., “History, Philosophy, Physics, and Future Directions of Aircraft Propulsion System/Inlet Integration,” in *Proceedings of ASME Turbo Expo 2004: Power for Land, Sea, and Air*, Jun. 2004, GT2004-54210, pp. 305–320.
- [12] D’Ambros, A., Kipouros, T., Zachos, P., Savill, M., and Benini, E., “Computational Design Optimization for S-Ducts,” *Designs*, vol. 2, no. 4, p. 36, 2018.
- [13] Das, I. and Dennis, J. E., “Normal-Boundary Intersection: A New Method for Generating the Pareto Surface in Nonlinear Multicriteria Optimization Problems,” *SIAM Journal on Optimization*, vol. 8, no. 3, pp. 631–657, 1998.

- [14] De Sturler, E., "Nested Krylov Methods Based on GCR," *Journal of Computational and Applied Mathematics*, vol. 67, no. 1, pp. 15–41, 1996.
- [15] De Sturler, E., "Truncation Strategies for Optimal Krylov Subspace Methods," *SIAM Journal of Numerical Analysis*, vol. 36, no. 3, pp. 864–889, 1999.
- [16] Del Rey Fernandez, D. C., Hicken, J. E., and Zingg, D. W., "Review of Summation-By-Parts Operators with Simultaneous Approximation Terms for the Numerical Solution of Partial Differential Equations," *Computers and Fluids*, vol. 95, pp. 171–196, 2014.
- [17] Drela, M., "Power Balance in Aerodynamic Flows," *AIAA Journal*, vol. 47, no. 7, pp. 1761–1771, 2009.
- [18] Felder, J. L., Kim, H. D., and Brown, G. V., "Turboelectric Distributed Propulsion Engine Cycle Analysis for Hybrid-Wing-Body Aircraft," in *47th AIAA Aerospace Sciences Meeting including The New Horizons Forum and Aerospace Exposition*, January 2009, AIAA 2009-1132.
- [19] Fidalgo, V. J., Hall, C. A., and Colin, Y., "A Study of Fan-Distortion Interaction Within the NASA Rotor 67 Transonic Stage," *Journal of Turbomachinery*, vol. 134, no. 5, 2012.
- [20] Frohnapfel, D. J., "Methodology Development and Investigation of Turbofan Engine Response to Simultaneous Inlet Total Pressure and Swirl Distortion," Ph.D. Thesis, Virginia Polytechnic Institute and State University, 2019.
- [21] Gagnon, H. and Zingg, D. W., "Two-Level Free-Form and Axial Deformation for Exploratory Aerodynamic Shape Optimization," *AIAA Journal*, vol. 53, no. 7, pp. 2015–2026, 2015.
- [22] Gill, P. E., Murray, W., and Saunders, M. A., "SNOPT: An SQP Algorithm for Large-Scale Constrained Optimization," *SIAM Review*, vol. 47, no. 1, pp. 99–131, 2005.
- [23] Goldberg, D., *Genetic Algorithms in Search, Optimization and Machine Learning*. Addison-Wesley, 1989.
- [24] Gray, J., Mader, C., Kenway, G., and Martins, J., "Coupled Aeropropulsive Optimization of a Three-Dimensional Boundary-Layer Ingestion Propulsor Considering Inlet Distortion," *Journal of Aircraft*, vol. 57, no. 6, pp. 1014–1025, 2020.
- [25] Guo, R. W. and Seddon, J., "An Investigation of the Swirl in an S-duct," *The Aeronautical Quarterly*, vol. 33, no. 1, pp. 25–58, 1982.
- [26] Hall, D. K., Huang, A. C., Uranga, A., Greitzer, E. M., Drela, M., and Sato, S., "Boundary Layer Ingestion Propulsion Benefit for Transport Aircraft," *Journal of Propulsion and Power*, vol. 33, no. 5, pp. 1118–1129, 2017.
- [27] Hamed, A. and Numbers, K., "Inlet Distortion Considerations for High Cycle Fatigue in Gas Turbine Engine," in *33rd Joint Propulsion Conference and Exhibit*, July 1997, AIAA 1997-3364.
- [28] Hercock, R. G., *Effects on Intake Flow Distortion on Engine Stability*. Paper 20 of AGARD-CP-324, 1982.
- [29] Hicken, J. E. and Zingg, D. W., "Parallel Newton-Krylov Solver for the Euler Equations Discretized using Simultaneous-Approximation Terms," *AIAA Journal*, vol. 46, no. 11, pp. 1695–1704, 2008.

- [30] Hicken, J. E. and Zingg, D. W., “A Simplified and Flexible Variant of GCROT for Solving Nonsymmetric Linear Systems,” *SIAM Journal of Scientific Computing*, vol. 32, no. 3, pp. 1672–1694, 2010.
- [31] Hicken, J. E. and Zingg, D. W., “Aerodynamic Optimization Algorithm with Integrated Geometry Parameterization and Mesh Movement,” *AIAA Journal*, vol. 48, no. 2, pp. 401–413, 2010.
- [32] Hui, Y., Feng, L., Yaoying, S., and Baigang, S., “Numerical Investigation of Electrohydrodynamic (EHD) Flow Control in an S-Shaped Duct,” *Plasma Science and Technology*, vol. 14, no. 10, pp. 897–904, 2012.
- [33] Jameson, A., Pierce, N. A., and Martinelli, L., “Optimum Aerodynamic Design using the Navier-Stokes Equations,” *Theoretical and Computational Fluid Dynamics*, vol. 10, pp. 213–237, 1998.
- [34] Joe, S. and Kuo, F., “Remarks on Algorithm 659: Implementing Sobol’s Quasirandom Sequence Generator,” *ACM Transactions on Math. Software*, vol. 29, no. 1, pp. 49–57, 2003.
- [35] Koo, D., Zingg, D. W., Chishty, W. A., and Ella, H. M. abo el, “Optimizing Intakes for Embedded Engines,” in *ISABE 2019*, September 2019, ISABE-2019-24290.
- [36] Küchemann, D. and Weber, J, *Aerodynamics of Propulsion*. New York: McGrawHill, 1953.
- [37] Lee, B. J. and Kim, C., “Automated Design Methodology of Turbulent Internal Flow using Discrete Adjoint Formulation,” *Aerospace Science and Technology*, vol. 11, no. 4, pp. 163–173, 2007.
- [38] Lee, D. S., Fahey, D. W., Skowron, A., Allen, R., M., Burkhardt, U., Chen, Q., Doherty, S. J., Freeman, S., Forster, P. M., Fuglestvedt, J., Gettelman, A., De León, R. R., Lim, L. L., Lund, M. T., Millar, R. J., Owen, B., Penner, J. E., Pitari, G., Prather, M. J., Sausen, R., and Wilcox, L. J., “The Contribution of Global Aviation to Anthropogenic Climate Forcing for 2000 to 2018,” *Atmospheric Environment*, vol. 4244, 2021.
- [39] Lee, D. S., Pitari, G., Grewe, V., Gierens, K., Penner, J. E., Petzold, A., Prather, M. J., Schumann, U., Bais, A., Berntsen, T., Iachetti, D., Lim, L. L., and Sausen, R., “Transport Impacts on Atmosphere and Climate: Aviation,” *Atmospheric Environment*, vol. 44, no. 37, pp. 4678–4734, 2010.
- [40] Liou, M. F., Kim, H., Lee, B., and Liou, M. S., “Aerodynamic Design of Integrated Propulsion–Airframe Configuration of a Hybrid Wing Body Aircraft,” *Shock Waves*, vol. 29, no. 8, pp. 1043–1064, 2019.
- [41] Lotter, K. W. and Jörg, J., “The Effect of Intake Flow Disturbances on APU Compressor Blade High Cycle Fatigue in the Airbus A300,” *ICAS-82-4.6.2*, pp. 1072–1081, Aug. 1982.
- [42] Ludwig, G., “Tomahawk Engine/Inlet Compatibility Study for F107-WR-400/402 Engines,” in Williams International Report CMEP 5003-2025, 1989.
- [43] Marble, F. E., “Three-Dimensional Flow in Turbomachines,” *High Speed Aerodynamics and Jet Propulsion*, vol. 10, pp. 83–166, 1964.

- [44] Meijerink, J. A. and van der Vorst, H. A., "An Iterative Solution Method for Linear Systems of Which the Coefficient Matrix is a Symmetric M-Matrix," *Mathematics of Computation*, vol. 31, no. 137, pp. 148–162, 1977.
- [45] Motycka, D. L., "Ground Vortex-Limit to Engine/Reverser Operation," *Journal of Engineering for Power*, vol. 98, no. 2, pp. 258–263, Apr. 1976.
- [46] Nocedal, J. and Wright, S. J., *Numerical Optimization*, 2nd ed. Springer, 2006.
- [47] Osusky, M. and Zingg, D. W., "A Parallel Newton-Krylov-Schur Flow Solver for the Navier-Stokes Equations Discretized Using Summation-By-Parts Operators," *AIAA Journal*, vol. 51, no. 12, pp. 2833–2851, 2013.
- [48] Owens, L. R., Allan, B. G., and Gorton, S. A., "Boundary-Layer-Ingesting Inlet Flow Control," *Journal of Aircraft*, vol. 45, no. 4, pp. 1431–1440, 2008.
- [49] Papadopoulos, F., Valakos, I., and Nikолос, I. K., "Design of an S-Duct Intake for UAV Applications," *Aircraft Engineering and Aerospace Technology*, vol. 84, no. 6, pp. 439–456, 2012.
- [50] Plas, A., Sargeant, M., Madani, V., Crichton, D., Greitzer, E., Hynes, T., and Ratio, H., "Performance of a Boundary Layer Ingesting (BLI) Propulsion System," in *45th AIAA Aerospace Sciences Meeting and Exhibit*, Jan. January 2007, AIAA 2007-450.
- [51] Ramachandra, S. M., Sudhakar, K., Perumal, P. V. K., and Jayashima, P., "Air-Inlet Engine Matching Problems Encountered in a Jet Trainer Re-Engining Program," *Journal of Aircraft*, vol. 19, no. 8, pp. 609–614, 1982.
- [52] Rashad, R. and Zingg, D. W., "Aerodynamic Shape Optimization for Natural Laminar Flow using a Discrete-Adjoint Approach," *AIAA Journal*, vol. 54, no. 11, pp. 3321–3337, 2016.
- [53] Reid, C., "The Response of Axial Flow Compressors to Intake Flow Distortion," in *Proceedings of ASME Turbo Expo 1969: Gas Turbine and Products Show*, Mar. 1969, 69-GT-29.
- [54] Roache, P. J., *Verification and Validation in Computational Science and Engineering*, 1st ed. Hermosa, 1998.
- [55] Seddon, J and Goldsmith, E. L., "Intake Aerodynamics," in ser. AIAA Education Series. AIAA, 1985.
- [56] Sederberg, T. W. and Parry, S. R., "Free-Form Deformation of Solid Geometric Models," *ACM SIGGRAPH Computer Graphics*, vol. 20, no. 4, pp. 151–160, 1986.
- [57] Smith, L. H., "Wake Ingestion Propulsion Benefit," *Journal of Propulsion and Power*, vol. 9, no. 1, pp. 74–82, 1993.
- [58] Sóbestor, A., "Tradeoffs in Jet Inlet Design: A Historical Perspective," *Journal of Aircraft*, vol. 44, no. 3, pp. 705–717, 2007.
- [59] Spalart, P. R., "Strategies for Turbulence Modeling and Simulations," *International Journal of Heat and Fluid Flow*, vol. 21, no. 3, pp. 252–263, 2000.
- [60] Streuber, G. and Zingg, D. W., "Evaluating the Risk of Local Optima in Aerodynamic Shape Optimization," *AIAA Journal*, vol. 59, no. 1, pp. 474–492, 2021.
- [61] Truong, A. H., Oldfield, C. A., and Zingg, D. W., "Mesh Movement for a Discrete-Adjoint Newton-Krylov Algorithm for Aerodynamic Optimization," *AIAA Journal*, vol. 46, no. 7, pp. 1695–1704, 2008.

- [62] Uranga, A., Drela, M., Greitzer, E. M., Hall, D. K., Titchener, N. A., Lieu, M. K., Siu, N. M., Casses, C., Huang, A. C., Gatlin, G. M., and Hannon, J. A., “Boundary Layer Ingestion Benefit of the D8 Transport Aircraft,” *AIAA Journal*, vol. 55, no. 11, pp. 3693–3708, 2017.
- [63] Uranga, A., Drela, M., Hall, D. K., and Greitzer, E. M., “Analysis of the Aerodynamic Benefit from Boundary Layer Ingestion for Transport Aircraft,” *AIAA Journal*, vol. 56, no. 11, pp. 4271–4281, 2018.
- [64] Vaccaro, J. C., Elimelech, Y., Chen, Y., Sahni, O., Jansen, K., and Amitay, M., “Experimental and Numerical Investigation of Steady Blowing Flow Control Within a Compact Inlet Duct,” *International Journal of Heat and Fluid Flow*, vol. 54, pp. 1143–1152, 2015.
- [65] “Vibration and Mission Simulation Testing on Engine 828 XF107-WR-400 Cruise Missile Engine,” Williams Research Corporation, Report No. 79-106-39, Tech. Rep., 1981.
- [66] Whitelaw, J. and Yu, S. M., “Turbulent Flow Characteristics in an S-Shaped Diffusing Duct,” *Flow Measurement and Instrumentation*, vol. 4, no. 3, pp. 171–179, 1993.
- [67] Willmer, A., Brown, T., and Goldsmith, E., *Effects of Intake Geometry on Circular Pitot Intake Performance at Zero and Low Forward Speeds*. AGARD-CP-301, 1981, ch. 5.
- [68] Wojewodka, M. M., White, C., Shahpar, S., and Kontis, K., “A Review of Flow Control Techniques and Optimisation in S-Shaped Ducts,” *International Journal of Heat and Fluid Flow*, vol. 74, pp. 223–235, 2018.
- [69] Xie, T. and Uranga, A., “Capturing Aero-Propulsive Coupling Effects With a Body-Force Propulsor Model,” in *AIAA Propulsion and Energy 2021 Forum*, August 2021, AIAA 2021-3456.
- [70] Yaras, M. I. and Grosvenor, A. D., “Evaluation of One- and Two-Equation Low-Re Turbulence Models. Part II - Vortex-Generator Jet and Diffusing S-Duct Flows,” *International Journal for Numerical Methods in Fluids*, vol. 42, no. 12, pp. 1321–1343, 2003.
- [71] Zhang, W., Knight, D., and Smith, D., “Automated Design of a Three-Dimensional Subsonic Diffuser,” *Journal of Propulsion and Power*, vol. 16, no. 6, pp. 1132–1140, 2000.
- [72] Zingg, D. W., Nemec, M., and Pulliam, T. H., “A Comparative Evaluation of Genetic and Gradient- Based Algorithms Applied to Aerodynamic Optimization,” *European Journal of Computational Mechanics/Revue Européene de Mécanique Numérique*, vol. 17, no. 1-2, pp. 103–126, 2008.